TECHNISCHE UNIVERSITÄT WIEN

DIPLOMA THESIS

Benchmark for the Eddy Current Problem in Laminated Iron Cores

Haik Jan Silm
Matriculation number: 0927299

November 11, 2016

Supervised by

Univ.Prof. Dr. techn. Joachim Schöberl
Dr. techn Karl Hollaus

Institute of Analysis and Scientific Computing

Submitted at

TU Wien
Faculty of Electrical Engineering
and Information Technology

Abstract

A new benchmark for the eddy current problem in laminated iron cores is designed to evaluate homogenization methods based on the finite element method. To this end the variational form is derived to solve the nonlinear problem. In this work, in extension to excite the coil with a current source, a voltage source is used and in this case the current is treated as an unknown. The solution method needs to be extended accordingly. To facilitate the modeling of the laminated iron core hexahedral finite elements have been employed. The Biot-Savart field has been exploited to avoid the modeling of the cylindrical coils. In summary, a nonlinear problem with network coupling is solved utilizing the Biot-Savart field. To calculate the time-domain solution the resulting nonlinear equation system consisting of over 16 million degrees of freedom is solved in each time step. A Newton method is used with a line search technique. The design procedure of the benchmark is described, highlighting the key requirements. The simulation results show that the requirements are fulfilled. Measurements taken from a simple setup are also presented.

Kurzfassung

Es wird ein neuer Benchmark für das Wirbelstromproblem in geschichteten Eisenkernen entworfen, um Methoden der Homogenisierung für die Finite-Element-Methode zu bewerten. Das Variationsproblem wird für den nichtlinearen Fall hergeleitet. Zusätzlich zur Verwendung eines eingeprägten Spulenstroms wird in dieser Arbeit, die Erregung der Spule mit einer Spannungsquelle betrachtet. Das Gleichungssystem und die Lösungsmethoden müssen entsprechend erweitert werden. Der geschichtete Eisenkern wird mit Hexaeder-Elementen diskritisiert. Das Biot-Savart-Feld der Spule wird verwendet um das Modellieren der Spulen zu vermeiden. Insgesamt wird ein nichtlineares Problem mit einem Netzwerk gekoppelt unter Einbeziehung des Biot-Savart-Feldes gelöst. Das resultierende nichtlineare Gleichungssystem hat über 16 Millionen Unbekannte und muss in jedem Zeitschritt gelöst werden. Dabei wird eine Newton- Methode mit einem Line Search Algorithmus verwendet. Der Entwurf vom Benchmark und die wesentlichen Anforderungen hervorgehoben. Die Simulationsergebnisse zeigen, dass die Anforderungen erfüllt werden. Weiters werden auch Messergebnisse von einer einfachen Anordnung präsentiert.

Danksagung

Als erstes möchte ich mich herzlich bei Herrn Prof. Joachim Schöberl vom Institut für Analysis und Scientific Computing für seine bereitwillige Unterstützung bedanken und, dass er sich bereit erklärt hat, diese Arbeit zu begutachten.

Besonders möchte ich mich bei Herrn Dr. Karl Hollaus bedanken, dass er diese Arbeit initiiert hat, für die finanzielle Unterstützung und für die umfassende Betreuung der Diplomarbeit.

Allen Kollegen in der Arbeitsgruppe möchte ich mich für die herzliche Aufnahme und ständige Unterstützung danken.

Wien, den 11. November 2016

Contents

1 Introduction **9**
- 1.1 FEM for laminated iron cores . . . 9
- 1.2 Benchmark problems . . . 10
- 1.3 Outline of the thesis . . . 10

2 The Eddy Current Problem **12**
- 2.1 Quasi-static magnetic field . . . 12
  - 2.1.1 Boundary value problem . . . 14
  - 2.1.2 Potential formulation . . . 16
- 2.2 Iron core properties . . . 17
  - 2.2.1 Commutation curve . . . 17
  - 2.2.2 Losses . . . 19
- 2.3 The finite element method . . . 19
  - 2.3.1 Discretization . . . 20
  - 2.3.2 Equation system . . . 20
  - 2.3.3 Uniqueness . . . 21

3 Benchmark Design **22**
- 3.1 Design of the benchmark dimensions . . . 23
  - 3.1.1 Parallel and serial configuration . . . 24
- 3.2 Specifications . . . 25
  - 3.2.1 Network . . . 25
  - 3.2.2 Lamination . . . 25
  - 3.2.3 Coils . . . 25

4 FEM-Model **29**
- 4.1 Time-stepping . . . 29
- 4.2 Nonlinear problem . . . 30
  - 4.2.1 Derivation from minimization problem . . . 30
  - 4.2.2 Newton's method for nonlinear FEM . . . 31
  - 4.2.3 Line search . . . 32
- 4.3 Network coupling . . . 33
  - 4.3.1 Separated Newton method . . . 34
- 4.4 Biot-Savart field . . . 35

5 Simulations **37**
5.1 Benchmark verification 37
5.1.1 Mesh and element order 37
5.1.2 Boundary conditions 38
5.1.3 Results 39
5.2 Measurements 43
5.2.1 Magnetic flux 43

6 Conclusion and Outlook **45**

List of Figures **46**

List of Tables **46**

Bibliography **47**

1 Introduction

1.1 FEM for laminated iron cores

Iron cores are one of the main components in electrical machines and transformers. Magnetic circuits with iron cores in their path have a low reluctance, because of the high permeability of iron, and are therefore are used to guide the magnetic field. If the magnetic field varies in time, the iron core is laminated to reduce the eddy currents, which would otherwise severely reduce the usability of the core.

Nowadays computational methods are employed for analyzing technical problems and for the design of new constructions. Simulation models are used advantageously both for the design and the optimization of transformers and electrical machines. An important application is the study of losses in a transformer and to develop means to reduce them. The use of computational methods to simulate the electric and thermal field and mechanic stresses in a transformer or a electrical machine, before it is actually built, poses a huge economical benefit. With more sophisticated simulation models with respect to accuracy and computational costs, these goals can be accomplished even better.

The finite element method (FEM) is one of the main computational methods to solve Maxwell's equations, the governing equations of the electromagnetic field. FEM is well suited for complex geometries and thus widely used. Since the early application of FEM for electromagnetic problems, considerable improvements to the methods have been made. Today, there exist a wide range of software implementations of FEM for electromagnetical problems.

The application of FEM in the context of laminated iron cores is still a challenging task. The thickness of the laminates are between 0.25 mm to 0.50 mm and they are isolated from each other by an extremely small air gap. The number of thin laminates ranges from a few hundreds to several thousands. To allow for each single laminate to be modeled with FEM would lead to a unfeasible number of degrees of freedom. The solution of the resulting equation system would require exorbitant computational effort.

The magnetic properties of laminated iron cores pose another challenge. They are strongly nonlinear, exhibit hysteresis and are anisotropic in case of grain orientated laminates. These properties are significant for the field distribution and subsequently for the losses. Therefore they have to be incorporated into the FEM model and require appropriate solution methods.

Homogenization methods are used to overcome these challenges. The aim is to abolish the need of modeling each laminate individually and to model the lamination as a bulk instead. This leads to a significant decrease of degrees of freedom. Many promising methods have been proposed, which are well suited for the complex iron cores ([1],[2],[3]).

1.2 Benchmark problems

Reference solutions are of great help to facilitate the development of homogenization methods. They are used for verification and also serve as a basis to develop new methods. Apart from numerical reference solutions, experimental validation is of great interest.

Since 1985 the International Compumag Society has published benchmark problems to promote the testing of computational electromagnetic methods. The well documented problems enable the scientific community to test their results and compare them to each other. Specifically TEAM Problem 21 [4] deals with the problem of modeling eddy currents in laminates. The problem consists of a stack of 20 silicon-steel laminates mounted above two excitation coils. Measurements of the resulting magnetic flux in a single laminate were obtained using search coils and the magnetic field density in the vicinity of the stack was scanned with a hall-sensor.

With regard to the simulation of transformers and electrical machines a benchmark problem with a laminated iron core composed of a higher number of laminates is still required. A numerical linear benchmark is presented in [5] and another numerical benchmark is proposed in [6] which takes the nonlinear magnetic properties of the core into account. Both benchmarks consist of a single iron stack with 556 and 200 laminates, respectively, and in a race-track shaped coil is used for excitation. Moreover, in [7] an experimental benchmark was measured consisting of an iron stack with 320 laminates and a circular coil. The average losses were determined but no measurements of the magnetic field were carried out and no reference solution was computed.

In the frame of the FWF-Project "Multi-Scale Finite Element Methods for Eddy Current Problems" (MSFEM4ECP) a new experimental benchmark is being developed to get a comprehensive benchmark problem. Measurements of the magnetic flux in the laminates, of the stray field and of the losses will be provided to the international scientific community. Furthermore, grain-oriented steel and step-lap joints will be part of the setup. A reference solution will be calculated using a high-performance computer. The benchmark will facilitate the development of the new homogenization approaches, which will deliver accurate solutions, but require only a fraction of the computer resources compared to standard FEM.

1.3 Outline of the thesis

In the frame of this thesis the new benchmark has been designed and numerical investigations have been carried using the open-source finite element library Netgen/NGSolve developed at the Institute of Analysis and Scientific Computing, TU Wien . Since Netgen/NGSolve is also used for simulations of large transformers, see Figure 1.1, its library includes efficient solvers for equation systems arising from electromagnetic problems [8]. In regard to the size of the benchmark problem efficient solvers were indispensable. The object-orientated design of NGSolve [9] also enables the easy implementation of additional methods which were required by the benchmark model.

In the second section the eddy current problem (ECP) is formulated. The equations of the quasi-magnetic field are presented and a boundary value problem is formulated using the magnetic vector potential. The commutation curve is introduced to model the magnetic nonlinearity of iron cores. Finally, the FEM formulation of the ECP is derived. The second third shows the benchmark design. After summarizing the requirements, a first hand assessment of the benchmark dimensions is made with simplified assumptions. Then the actual specifications are presented. In the fourth section the tools used for the nonlinear problem are introduced. Additional methods which are necessary to model the benchmark are derived, including network coupling with FEM and how the coils can be represented by the Biot-Savart field. Simulation results presented in section 5 show that the requirements are fulfilled by the benchmark design. Simple measurements by means of a small setup are also provided.

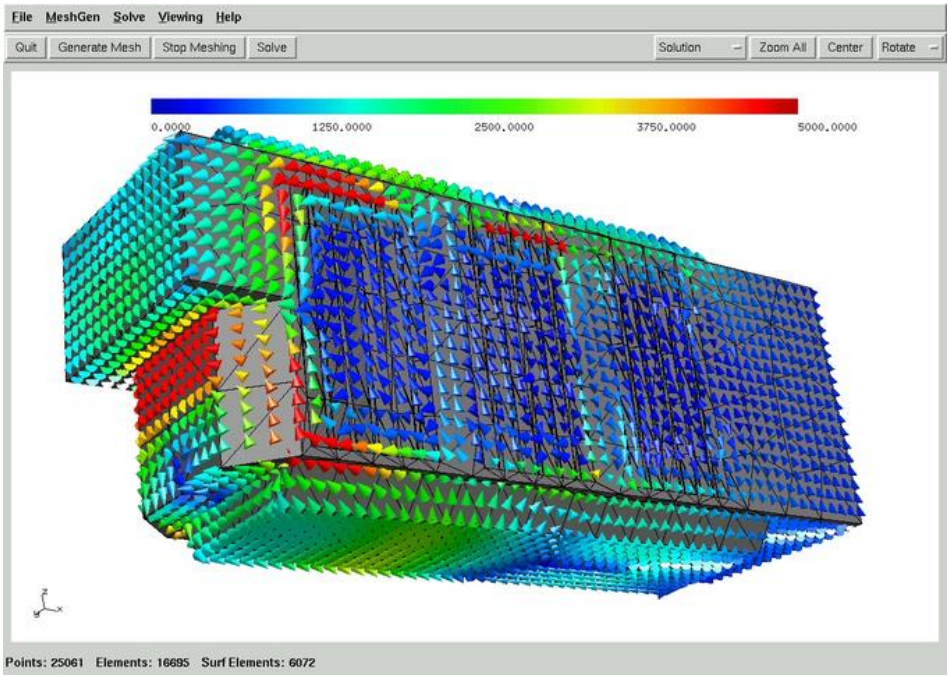

Figure 1.1. Eddy current simulation in a transformer with Netgen/NGSolve.

2 The Eddy Current Problem

Mathematical models do not precisely reflect reality, but are simplifications which do not take into account all physical effects. which is feasibly when for example only the heat losses are of interest. In the setting of the benchmark the eddy current problem (ECP) describes the electromagnetic field and subsequently the losses in the benchmark. Physical laws and empirical models together with measurement results are used to derive the mathematical model.

In this section the ECP is formulated as a boundary value problem (BVP) and it is shown how nonlinear magnetic material properties are taken into consideration. Later FEM is introduced as a method to solve the BVP approximately.

2.1 Quasi-static magnetic field

Gauss' law for magnetism states that the *magnetic flux* Φ through a closed surface ∂V of a volume V is zero

$$\Phi(\partial V) = 0. \tag{2.1.1}$$

Using the *magnetic flux density* $\boldsymbol{B}$ this reads in integral form as

$$\int_{\partial V} \boldsymbol{B} \cdot \boldsymbol{n} \, \mathrm{d}S = 0, \tag{2.1.2}$$

where $\boldsymbol{n}$ denotes the normal vector of the surface element $\mathrm{d}S$. The *Divergence theorem* states that

$$\int_{\partial V} \boldsymbol{B} \cdot \boldsymbol{n} \, \mathrm{dS} = \int_{V} \operatorname{div} \boldsymbol{B} \, \mathrm{d}V \tag{2.1.3}$$

and since (2.1.2) holds for any volume V,

$$\operatorname{div} \boldsymbol{B} = 0 \tag{2.1.4}$$

is valid. The law (2.1.4) states, that there exist no magnetic sources and magnetic fields always form closed loops. Considering an interface Γ_i of two subdomains Ω_1 and Ω_2, the interface condition

$$\boldsymbol{n} \cdot (\boldsymbol{B}_1 - \boldsymbol{B}_2) = 0 \tag{2.1.5}$$

can be derived, where $\boldsymbol{B}_1$ and $\boldsymbol{B}_2$ denote the limit of the flux density when approaching Γ_i from the subdomain Ω_1 and Ω_2, respectively, see Figure 2.1. This means that the normal component of $\boldsymbol{B}$ is always continuous.

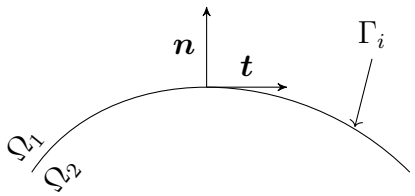

Figure 2.1. Interface Γ_i between the subdomains Ω_1 and Ω_2 with normal vector $\boldsymbol{n}$ and tangential vector $\boldsymbol{t}$.

According to *Faraday's law* a time dependent Φ through a surface S yields the *electric voltage*

$$U(\partial S) = -\frac{\mathrm{d}}{\mathrm{d}t}\Phi(S) \tag{2.1.6}$$

around the contour ∂S of the surface. This is equal to

$$\int_{\partial S} \boldsymbol{E} \cdot \boldsymbol{t} \,\mathrm{d}l = -\int_{S} \frac{\partial \boldsymbol{B}}{\partial t} \cdot \boldsymbol{n} \,\mathrm{d}S \tag{2.1.7}$$

for surfaces which are constant in time, where $\boldsymbol{E}$ is the *electric field strength*, $\boldsymbol{t}$ is the tangential vector of ∂S and $\frac{\partial \boldsymbol{B}}{\partial t}$ denotes the partial derivative of $\boldsymbol{B}$ with respect to time. *Stokes theorem* leads to

$$\int_{\partial S} \boldsymbol{E} \cdot \boldsymbol{t} \,\mathrm{d}l = \int_{S} \operatorname{curl} \boldsymbol{E} \cdot \boldsymbol{n} \,\mathrm{d}S. \tag{2.1.8}$$

Since (2.1.7) holds for any surface it follows that

$$\operatorname{curl} \boldsymbol{E} = -\frac{\partial \boldsymbol{B}}{\partial t}. \tag{2.1.9}$$

The interface conditions

$$\boldsymbol{n} \times (\boldsymbol{E}_1 - \boldsymbol{E}_1) = \boldsymbol{0} \tag{2.1.10}$$

can be derived from (2.1.7), where $\boldsymbol{E}_1, \boldsymbol{E}_2$ are defined similarly to $\boldsymbol{B}_1, \boldsymbol{B}_2$. It states that the tangential component of $\boldsymbol{E}$ is continuous across each interface.

Ampère's law states that the *magnetomotive force* $\mathcal{F}$ on ∂S equals to the *current linkage* Θ through S

$$\mathcal{F}(\partial S) = \Theta(S). \tag{2.1.11}$$

For coils Θ equals the number of windings N times the *electric current* I in the wire of the coil

$$\Theta(S) = NI. \tag{2.1.12}$$

Using the *magnetic field strength* $\boldsymbol{H}$ and the *current density* $\boldsymbol{J}$ (2.1.11) can be written in integral form

$$\int_{\partial S} \boldsymbol{H} \cdot \boldsymbol{t} \,\mathrm{d}l = \int_{S} \boldsymbol{J} \cdot \boldsymbol{n} \,\mathrm{d}S. \tag{2.1.13}$$

Using *Stokes theorem* and the same argumentation as for (2.1.9) leads to

$$\operatorname{curl} \boldsymbol{H} = \boldsymbol{J}. \tag{2.1.14}$$

Taking a surface current density $\boldsymbol{K}$ on Γ_i into account, the interface condition is

$$\boldsymbol{n} \times (\boldsymbol{H}_1 - \boldsymbol{H}_2) = \boldsymbol{K}. \tag{2.1.15}$$

This means, that if no surface currents are present, the tangential component of $\boldsymbol{H}$ is continuous.

The equations (2.1.4), (2.1.9) and (2.1.14) are a system of partial differential (PDE) equations describing the *quasi-static magnetic field*:

$$\operatorname{curl} \boldsymbol{H} = \boldsymbol{J} \tag{2.1.16a}$$

$$\operatorname{curl} \boldsymbol{E} = -\frac{\partial \boldsymbol{B}}{\partial t} \tag{2.1.16b}$$

$$\operatorname{div} \boldsymbol{B} = 0 \tag{2.1.16c}$$

This set is a simplification of *Maxwell's equations*, since the *displacement currents* are neglected in *Ampère's law*. This restriction is admissible for transformers and electrical machines operating at a *frequency* f of 50 Hz.

The physical laws (2.1.16) are to be combined with constitutive equations that describe the relation of the field quantities $\boldsymbol{H}, \boldsymbol{J}, \boldsymbol{E}$ and $\boldsymbol{B}$ for a specific material. When solving technical problems, continuum models are used to describe the material properties. The relationship between the magnetic field quantities can be expressed as

$$\boldsymbol{B} = \mu \boldsymbol{H} \tag{2.1.17}$$

with the *magnetic permeability* μ. Together with Ohm's law

$$\boldsymbol{J} = \sigma \boldsymbol{E}, \tag{2.1.18}$$

where σ is the *electric conductivity*, the system of equations (2.1.16) is coupled. The permeability μ is further discussed in section 2.2. For now, it should be noted that μ can be represented by either a scalar value, a tensor or a function of $\boldsymbol{H}$ in case of a nonlinear magnetic material. The choice determines which physical effects are accounted for in the model. Likewise, σ is usually a scalar, but for example when modeling periodical materials as a bulk, σ becomes a tensor [10].

2.1.1 Boundary value problem

To compute the electromagnetic field for a laminated iron core, solutions of (2.1.16) together with the constitutive relations (2.1.17) and (2.1.18) are looked for. Therefore, the region will be encompassed by a bounded domain Ω and the exterior of Ω is considered by boundary conditions on the boundary $\Gamma = \partial\Omega$.

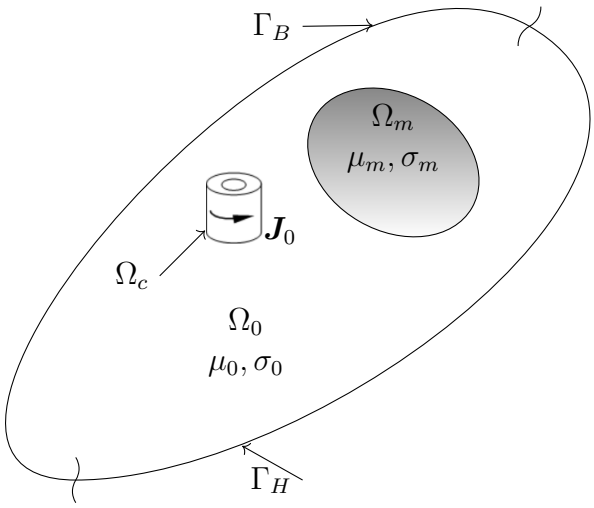

Figure 2.2. Bounded domain $\Omega = \Omega_0 \cup \Omega_m$ with the boundary $\Gamma = \Gamma_{\boldsymbol{H}} \cup \Gamma_{\boldsymbol{B}}$.

In the derivation of the ECP a domain Ω consisting of a conducting and a non-conducting medium is considered. To take into account a space-dependent μ and σ, Ω is divided into non-overlapping subdomains.

$$\Omega = \Omega_0 \cup \Omega_m, \tag{2.1.19}$$

where each subdomain represents a specific medium. The subdomain Ω_0 represents air. Its electric conductivity σ_0 is zero and the permeability μ_0 equals the permeability of free space, see section 2.2. The subdomain Ω_m represents iron with a permeability of μ_m and electric conductivity σ_m.

A prescribed current density $\boldsymbol{J}_0$ is used in $\Omega_c \subset \Omega_0$, to model a current carrying coil, see Figure 2.2. This is a simplification, as it models a current in the wire, but the skin-effect and proximity effect on the current density distribution is neglected. This simplification is acceptable in the setting of the ECP, because mainly the solution in the conducting medium is of interest and it can be expected that the actual current density distribution in the coil is not decisive for the solution in Ω_m.

The boundary is divided into two parts

$$\Gamma = \Gamma_H \cup \Gamma_B, \tag{2.1.20}$$

according to the applied boundary conditions. Due to the different continuity conditions (2.1.5), (2.1.10) and (2.1.15), the tangential components or normal components can be prescribed, which model different properties of the exterior.

For the benchmark the boundary conditions will fulfill two functions. First of all, the benchmark is modeled as if it was independent from the surroundings. Theoretically, this would mean that the air domain Ω_0 is unlimited. This would make the problem

infinitely large, which is not feasible in practice. Instead a finite surrounding domain is modeled. The boundary conditions are chosen to keep the distortion compared to the unbounded solution minimal. It can be expected that the electromagnetic field will decay to zero for points far away from the benchmark. Therefore it is intuitive to set the field values to zero:

$$\boldsymbol{H} \times \boldsymbol{n} = \boldsymbol{0} \quad \text{on} \quad \Gamma_H \tag{2.1.21}$$

$$\boldsymbol{B} \cdot \boldsymbol{n} = 0 \quad \text{on} \quad \Gamma_B \tag{2.1.22}$$

Ultimately, it does not matter which condition is imposed, because if the boundary is sufficiently far away it does not effect the solution close to Ω_m.

Secondly, boundary conditions can be used to simplify problems which have planes of symmetries. In this case it is possible to model only a part of the problem. Appropriate boundary conditions enforce the correct symmetry of the solution.

2.1.2 Potential formulation

To arrive at a simpler mathematical form of (2.1.16), (2.1.17) and (2.1.18) which is suitable for FEM, various potential formulations can be employed [11]. In this work the formulation with a *magnetic vector potential* $\boldsymbol{A}$ introduced by

$$\boldsymbol{B} = \operatorname{curl} \boldsymbol{A} \tag{2.1.23}$$

is used. Since

$$\operatorname{div} \operatorname{curl} \boldsymbol{A} = 0 \tag{2.1.24}$$

holds, (2.1.16c) is fulfilled. Note that $\boldsymbol{A}$ is not uniquely defined by (2.1.23), because it is possible to add a gradient field to $\boldsymbol{A}$ without changing $\boldsymbol{B}$.

Inserting (2.1.23) in (2.1.9) yields

$$\operatorname{curl} \boldsymbol{E} = -\frac{\partial \operatorname{curl} \boldsymbol{A}}{\partial t} \tag{2.1.25}$$

$$\boldsymbol{E} = -\frac{\partial \boldsymbol{A}}{\partial t} - \operatorname{grad} \phi \tag{2.1.26}$$

with an electric scalar potential ϕ. Since only $\boldsymbol{B}$ is of interest, a solution of $\boldsymbol{A}$ is chosen, which already incorporates $\operatorname{grad} \phi$, so

$$\boldsymbol{E} = -\frac{\partial \boldsymbol{A}}{\partial t}. \tag{2.1.27}$$

With (2.1.14), (2.1.17), (2.1.18) and (2.1.27) a second order parabolic PDE for the unknown vector potential $\boldsymbol{A}$ in Ω can be derived:

$$\operatorname{curl} \mu^{-1} \operatorname{curl} \boldsymbol{A} + \sigma \frac{\partial \boldsymbol{A}}{\partial t} = \boldsymbol{J_0} \quad \text{in} \quad \Omega \tag{2.1.28}$$

Suitable boundary conditions for $\boldsymbol{A}$ have to be formulated for a unique solution of (2.1.28). The boundary conditions (2.1.21) and (2.1.22) yield

$$\mu^{-1} \operatorname{curl} \boldsymbol{A} \times \boldsymbol{n} = \boldsymbol{0} \quad \text{on} \quad \Gamma_N \tag{2.1.29a}$$

$$\boldsymbol{A} \times \boldsymbol{n} = \boldsymbol{0} \quad \text{on} \quad \Gamma_D \tag{2.1.29b}$$

The boundary condition on $\Gamma_N = \Gamma_H$ is of Neumann type, i.e. the derivative of the solution is specified, and on $\Gamma_D = \Gamma_B$ is of Dirichlet type, i.e. its value is specified. In Ω_0 the PDE (2.1.28) degenerates to an elliptic problem, since the second term on the left hand side vanishes. This requires further consideration to obtain a unique solution, see section 2.3.3.

2.2 Iron core properties

In the simplest case the magnetic properties of a material are linear and isotropic and the relationship

$$\boldsymbol{B} = \mu_r \mu_0 \boldsymbol{H} \tag{2.2.1}$$

is used. The permeability of free space $\mu_0 = 4\pi 10^{-7}\,\mathrm{Vs/Am}$ is a natural constant and the relative permeability μ_r depends on the material (for air $\mu_r = 1$). Materials can be classified as diamagnetic materials and paramagnetic materials with $\mu_r < 1$ and $\mu_r > 1$, respectively. Iron belongs to a third category, the so called ferromagnetic materials. For ferromagnetic materials the simple relation (2.2.1) fails.

A typical relationship between the magnitudes $H = |\boldsymbol{H}|$ and $B = |\boldsymbol{B}|$ of a ferromagnetic material is shown Figure 2.3. Using a field dependent permeability $\mu_m(H)$ the characteristic magnetic properties of iron can be summarized by two effects. First of all, $\mu_m(H)$ is very high in comparison to μ_0 for small values of H. This changes once the saturation level of the material is reached. From there on the increase of B for increasing H will be similar to that of in air. This effect stems from the Weiss domains of iron, which align themselves in the direction of the applied field [12]. Secondly, hysteresis occurs in iron. Simply speaking hysteresis means that $\mu_m(H)$ is not unique for a specific H, but depends on its history. A typical hysteresis loop with an initial magnetization curve along with the characteristic quantities, the coercivity H_c and the saturation remanence B_r, is shown in Figure 2.3. Arrows display the direction the loop is passed through.

2.2.1 Commutation curve

If saturation effects and hysteresis are disregarded, a linear approximation of the B–H relationship (2.2.1) is used for computations, which assign a very high μ_r to iron. Of course a constant μ_r is only feasible if saturation is not significant. If the linear approximation is not justified, modeling the nonlinear relationship becomes necessary. This can be accomplished using the *magnetization curve* of the material. The magnetization curve sets up a unique relationship between measurement values of B and H, thus hysteresis is neglected.

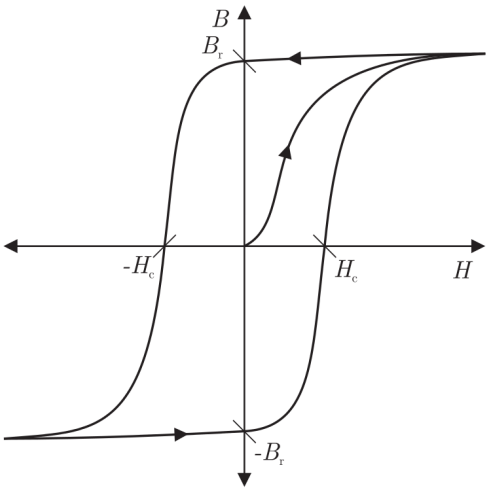

Figure 2.3. Characteristic behavior of the ferromagnetic material.

In contrast to the initial magnetization curve, which is used for magnetostatic problems, the commutation curve is chosen to consider the magnetic material in the ECP. The commutation curve can be obtained by measurements using an Epstein frame [13]. A single frequency is used for the excitation and the amplitude is increased in discrete steps. After a transient process, which depends on the previous state of the material, for each amplitude closed loops of the B–H relationship are measured. The commutation curve is the connection of the peak values of each loop, see Figure 2.4.

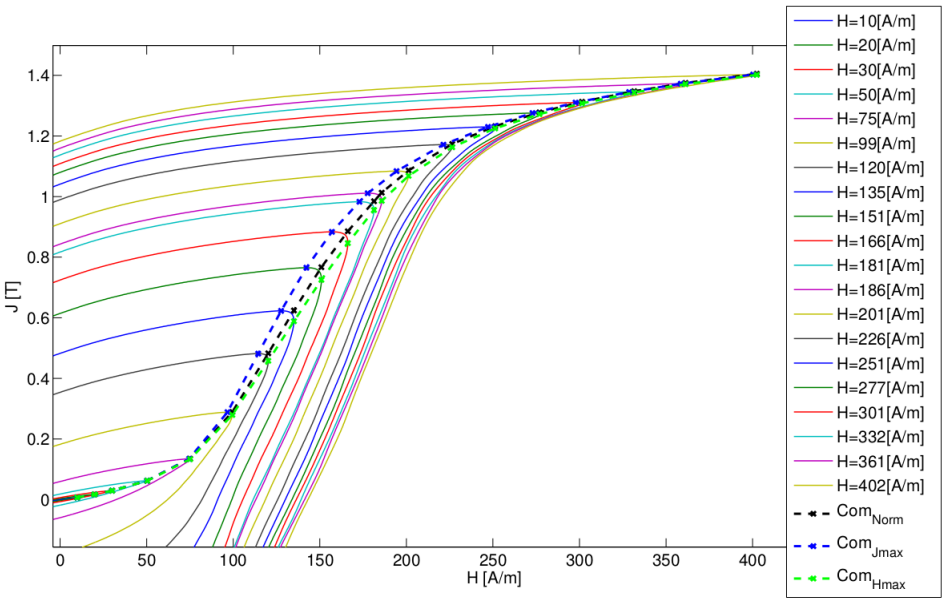

Figure 2.4. Commutation curve of a laminate measured with an Epstein frame [13].

2.2.2 Losses

Three types of iron losses are distinguished. First of all, the *eddy current losses*, can be calculated using the eddy current loss density

$$p = \boldsymbol{E} \cdot \boldsymbol{J}. \tag{2.2.2}$$

The total eddy current losses equal

$$P = \int_{\Omega_m} p \, \mathrm{d}\Omega. \tag{2.2.3}$$

Inserting (2.1.27) and (2.1.18) into (2.2.2) shows, that the eddy currents are quadratic in the magnetic field and in the frequency.

The *hysteresis losses* are equal to the area of a closed hysteresis loop. They are quadratic in the magnetic field, but linear in the frequency. Clearly, the hysteresis losses are not accounted for in simulation, which use the commutation curve. A possible approach to this problem is to add a post-processing step, where specific loss curves are used to estimate the total losses [7]. Finally, all other losses are summed up as *excess losses*.

2.3 The finite element method

The PDE (2.1.28) is not analytically solvable for a complicated BVP. Only for simplified problems, like a semi-infinite medium, it is possible to derive a closed form expression for the solution. Technical problems mostly do not submit themselves to those idealizations. Therefore numerical methods like FEM are employed. In most cases the solution will be an approximation, as the computational method has to reduce the problem to a finite number of unknown.

As it was shown from the transformation of the global laws (2.1.2), (2.1.7) and (2.1.11) to the BVP (2.1.28), different formulations can be used for the ECP. The various computational methods are based on different formulations. For example the finite difference method uses the PDE (2.1.28) directly. FEM is based on the *weak formulation*.

In the following, the notation

$$\nu := \mu^{-1} \tag{2.3.1}$$

with the *magnetic reluctivity* ν will be used. The weak formulation, also called variational form, can be derived from the method of weighted residuals or from a variation principle [14]. Multiplying (2.1.28) by a suitable test function $\boldsymbol{v}$ and integrating over Ω by parts yields

$$\int_{\Omega} \nu \operatorname{curl} \boldsymbol{A} \cdot \operatorname{curl} \boldsymbol{v} \, \mathrm{d}\Omega + \frac{\partial}{\partial t} \int_{\Omega} \sigma \boldsymbol{A} \cdot \boldsymbol{v} \, \mathrm{d}\Omega = \int_{\Omega} \boldsymbol{J}_0 \cdot \boldsymbol{v} \, \mathrm{d}\Omega + \int_{\Gamma} (\nu \operatorname{curl} \boldsymbol{A} \times \boldsymbol{n}) \cdot \boldsymbol{v} \, \mathrm{d}\Gamma. \tag{2.3.2}$$

The weak form of the BVP (2.1.28),(2.1.29) is:
Find $\boldsymbol{A} \in V_g := \{\boldsymbol{A} \in H(\mathrm{curl}, \Omega) \,|\, \boldsymbol{A} \times \boldsymbol{n} = 0 \text{ on } \Gamma_D\}$, such that

$$\int_\Omega \nu \,\mathrm{curl}\, \boldsymbol{A} \cdot \mathrm{curl}\, \boldsymbol{v} \,\mathrm{d}\Omega + \frac{\partial}{\partial t} \int_\Omega \sigma \boldsymbol{A} \cdot \boldsymbol{v} \,\mathrm{d}\Omega = \int_\Omega \boldsymbol{J}_0 \cdot \boldsymbol{v} \,\mathrm{d}\Omega \tag{2.3.3}$$

for all $\boldsymbol{v} \in V_0 := \{\boldsymbol{v} \in H(\mathrm{curl}, \Omega) \,|\, \boldsymbol{v} \times \boldsymbol{n} = \boldsymbol{0} \text{ on } \Gamma_D\}$.

The Hilbert-Space $H(\mathrm{curl}, \Omega)$ is the space of all vector valued functions for which the weak curl exists. These have a continuous tangential component in Ω. The boundary condition (2.1.29b) is accounted for in the choice of the subspaces for $\boldsymbol{v}$ and $\boldsymbol{A}$. The elements of the subspace V_g are the members of $H(\mathrm{curl}, \Omega)$ which fulfill the Dirichlet boundary condition and V_0 are the test functions which are zero on the Dirichlet boundary Γ_D. Together with the homogeneous Neumann conditions (2.1.29a) on Γ_N, the boundary integral in (2.3.2) vanishes.

2.3.1 Discretization

FEM uses a partition of the domain Ω into non-overlapping subdomains Ω_j called FE mesh. Each subdomain Ω_j is called a finite element (FE). . For each element shape functions $\boldsymbol{\varphi}_i$ are defined, which have a finite support, that is to say, they are non-zero only in some neighborhood of Ω_j. The shape functions belong to a N_{DoF}-dimensional subspace $V_h \subset H(\mathrm{curl}, \Omega)$ and form a basis for the approximation of $\boldsymbol{A}$ of the form

$$\boldsymbol{A}_h := \sum_{j=1}^{N_{\mathrm{DoF}}} u_j \boldsymbol{\varphi}_j \tag{2.3.4}$$

with unknown coefficient values u_i. The test functions $\boldsymbol{v}$ are selected from the same subspace V_h (the so called Galerkin-method).

The weak formulation of the finite element approximation $\boldsymbol{A}_h$ is therefore:
Find $\boldsymbol{A}_h \in V_{g,h} = \{\boldsymbol{A} \in V_h \,|\, \boldsymbol{A} \times \boldsymbol{n} = \boldsymbol{0} \text{ on } \Gamma_D\}$, such that

$$\int_\Omega \nu \,\mathrm{curl}\, \boldsymbol{A}_h \cdot \mathrm{curl}\, \boldsymbol{v} \,\mathrm{d}\Omega + \frac{\partial}{\partial t} \int_\Omega \sigma \boldsymbol{A}_h \cdot \boldsymbol{v} \,\mathrm{d}\Omega = \int_\Omega \boldsymbol{J}_0 \cdot \boldsymbol{v} \,\mathrm{d}\Omega \tag{2.3.5}$$

for all $\boldsymbol{v} \in V_{0,h} = \{\boldsymbol{v} \in V_h \,|\, \boldsymbol{v} \times \boldsymbol{n} = \boldsymbol{0} \text{ on } \Gamma_D\}$.

2.3.2 Equation system

Inserting (2.3.4) into (2.3.5) yields

$$\int_\Omega \nu \left(\sum_{j=1}^{N_{\mathrm{DoF}}} u_j \,\mathrm{curl}\, \boldsymbol{\varphi}_j \right) \cdot \mathrm{curl}\, \boldsymbol{v} \,\mathrm{d}\Omega + \frac{\partial}{\partial t} \int_\Omega \sigma \left(\sum_{j=1}^{N_{\mathrm{DoF}}} u_j \boldsymbol{\varphi}_j \right) \cdot \boldsymbol{v} \,\mathrm{d}\Omega = \int_\Omega \boldsymbol{J}_0 \cdot \boldsymbol{v} \,\mathrm{d}\Omega. \tag{2.3.6}$$

Testing with the N_{DoF} test functions $\boldsymbol{\varphi}_i$ leads to the FE equation system

$$\mathbf{S}\boldsymbol{u} + \mathbf{M}\frac{\partial \boldsymbol{u}}{\partial t} = \boldsymbol{f} \tag{2.3.7}$$

for the unknown vector $\boldsymbol{u} = [u_1, \ldots, u_{N_{\mathrm{DoF}}}]^{\mathrm{T}}$. The matrix $\mathbf{S} \in \mathbb{R}^{N_{\mathrm{DoF}} \times N_{\mathrm{DoF}}}$ with entries

$$S_{ij} = \int_{\Omega} \nu \operatorname{curl} \boldsymbol{\varphi}_i \cdot \operatorname{curl} \boldsymbol{\varphi}_j \, \mathrm{d}\Omega \tag{2.3.8}$$

is called the stiffness matrix, $\mathbf{M} \in \mathbb{R}^{N_{\mathrm{DoF}} \times N_{\mathrm{DoF}}}$ with entries

$$M_{ij} = \int_{\Omega} \sigma \boldsymbol{\varphi}_i \cdot \boldsymbol{\varphi}_j \, \mathrm{d}\Omega \tag{2.3.9}$$

is called the mass matrix and the right hand side vector $\boldsymbol{f} \in \mathbb{R}^{N_{\mathrm{DoF}}}$ with elements

$$f_i = \int_{\Omega} \boldsymbol{J}_0 \cdot \boldsymbol{\varphi}_i \, \mathrm{d}\Omega \tag{2.3.10}$$

is called load vector.

2.3.3 Uniqueness

The fact that $\boldsymbol{A}$ is not uniquely defined in Ω_0, where $\sigma = 0$, can be overcome by assigning a small conductivity $\sigma_\epsilon \ll \sigma_m$ to Ω_0. This σ_ϵ is called a regularization term, because using the term yields a regular equation system.

The regularization term must not be too large in order to not severely distort the solution. At the same time it has to be large enough for the finite-precision arithmetic of the machine. The resulting coefficient matrix still has an unfavorable condition number. This limits the convergence rate of iterative solvers and consequently appropriate preconditioners have to be used.

3 Benchmark Design

The benchmark consists of a laminated iron core and two cylindrical coils as shown in Figure 3.1. The iron core is made of four equal iron stacks that are separated by thin air gaps and are positioned perpendicular to each other. The coils are equal and are arranged symmetrically at the limbs.

The iron core provides a path with low reluctance for the magnetic field. This arrangement was preferred over a single stack with a coil, which has very high reluctance. To generate high fluxes a high magnetomotive force would have been necessary. This would have limited the applicability of the benchmark in a laboratory with standard equipment.

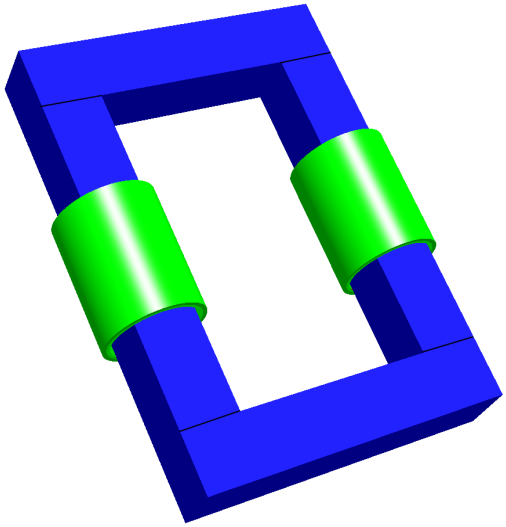

Figure 3.1. Design of the benchmark with four iron stacks (blue) and two coils (green).

An important benefit of using a second coil is that the benchmark has three planes of symmetry. Therefore only one eighth of the benchmark has to be modeled. Another advantage is that the measurements can be crosschecked in different locations. Furthermore, negative coupling of the coils can be achieved by reversing the connection of one coil. The magnetic fields of each coil are then opposed, which enforces a high stray field.

A voltage source is used to drive the magnetic field of the benchmark. Since only a fixed sinusoidal voltage is available, a series resistor has to be used to reduce the inrush current. Moreover, the resistor limits the current when the impedance of the benchmark arrangement is too low in the case of negative coupling or when the iron core is in saturation.

Additionally, this arrangement is extendable. One proposal would be to turn the yokes by 90 degrees, so that the surface of their laminates are perpendicular to the limbs. In this case the effect of a magnetic flux normal to the laminates would be more pronounced. Another interesting extension would be to use step-lap joints to connect the limbs with the yokes.

3.1 Design of the benchmark dimensions

To design the benchmark the following constraints and requirements were taken into account:

1. A reasonable number of laminates should be used for each stack. This is important for the benchmark to be a good reference for homogenization methods. Homogenization methods perform best when the iron core has many laminates.

2. The iron core should be operated in the saturated state. In this case the nonlinearity of the magnetization curve cannot be neglected in the model and a nonlinear problem has to be solved.

3. The overall field should exhibit enough stray flux so measurements of the magnetic flux density close to the core with a hall-sensor are attainable.

4. The power required to achieve saturation has to be available in the laboratory.

Figure 3.2 shows the setup of the benchmark with a series resistor connected to the voltage source. In the laboratory the amplitude of the source voltage is fixed and the current I is limited. The series resistor will additionally reduce the voltage available for the benchmark U_{BM} by the voltage drop on R

$$U_{\mathrm{BM}} = U_0 - RI. \tag{3.1.1}$$

In the following discussion it will be assumed that the benchmark is operated in saturation. Looking at the magnetization curve in Figure 2.4, this defines a operating point with B_{sat}. For simplicity it is assumed that if $B < B_{\mathrm{sat}}$ holds in the core, the benchmark is linear with $\mu_m \gg \mu_0$.

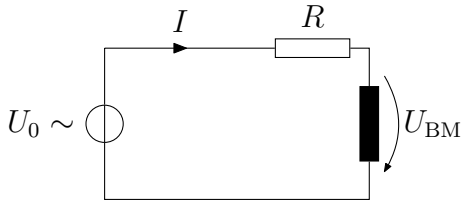

Figure 3.2. Network coupling of the benchmark with an AC voltage source U_0 and a series resistor R.

With A being the cross-section of the core, the flux in the core is

$$\Phi = AB_{\text{sat}}. \tag{3.1.2}$$

The multiplication is made under the assumption, that the flux distribution is approximately homogeneous in the cross section of the core.

Together with the available U_{BM} from (3.1.1) and the required Φ from (3.1.2) the maximum number of turns N_c for each coil can be determined. To this end it is assumed that almost every winding is linked with Φ. In the linear case U_{BM} is sinusoidal with the frequency f and Faraday's law yields

$$N_c \approx \frac{\sqrt{2}U_{\text{BM}}}{2\pi f \Phi}. \tag{3.1.3}$$

If the actual number of turns is chosen much higher than N_c, the saturation point will not be reached for the whole core. On the other hand, less turns will amplify the saturation of the iron core.

Depending on the magnetic reluctance $\mathcal{R}_m$, a certain magnetomotive force $\mathcal{F}$ is required for Φ in the iron core

$$\mathcal{R}_m = \frac{\mathcal{F}}{\Phi}. \tag{3.1.4}$$

This is an analogy to Ohm's law for magnetic circuits. The technical limitation for I and the number of windings N_c restrict the magnetomotive force to

$$\mathcal{F} = IN_c. \tag{3.1.5}$$

With the assumption $\mu_m \gg \mu_0$, the reluctance of the air gaps is dominant

$$\mathcal{R}_m \approx 4\mu_0 \frac{l_0}{A}. \tag{3.1.6}$$

With (3.1.6) the choice for the air gap width l_0 is restricted.

The above design procedure is of course based on many simplifications, e.g. neglecting nonlinear effects. In reality $\mathcal{R}_m$ depends on the actual magnetic field. When Φ is high, $\mathcal{R}_m$ will rise abruptly. Due to (3.1.4) and (3.1.5) I rises accordingly. It will not be sinusoidal anymore, but will have peaks when the core is in the saturated state. Consequently, U_{BM} is not sinusoidal and is reduced due to the voltage drop on the resistor. This will reduce further magnetization of the iron core and hence I is damped.

3.1.1 Parallel and serial configuration

The two coils can either be connected in parallel to the source or in series. For the parallel arrangement (3.1.3) is still valid for each coil, since both carry the same flux Φ. If the coils are connected in series N_c is half of the value compared to the parallel case for the same Φ, because U_{BM} is divided between the two coils. Thus, the change of the topology from parallel to series can be used to conveniently reduce the magnetization of the iron core.

This can be exploited in the case of negative coupling, when the magnetic flux will hardly enter the yokes and will flow mostly in air. The resulting $\mathcal{R}_m$ in this setting is very high. Thus it is necessary to reduce Φ, because of the limitation (3.1.5). At the same time, if the coils are in series there is twice the amount of $\mathcal{F}$ available for the same I compared to the parallel connection.

3.2 Specifications

3.2.1 Network

The laboratory intended for the measurements belongs to the Institute for Mechanics and Mechatronics at TU Wien. Its voltage source provides $U_{0,\text{eff}} = 400\,\text{V}$ with a maximum current output of $I_{\text{max,eff}} = 30\,\text{A}$. The benchmark dimensions and the coils were selected in accordance with these limitations. In the case of positive coupling, the coils are to be connected in parallel and a series resistor of $R = 2.2\,\Omega$ is used. In the case of negative coupling, the coils are to be connected in series and a series resistor of $R = 10\,\Omega$ is used.

3.2.2 Lamination

The yokes and limbs of the magnetic circuit are made up of $N = 183$ laminates of type M400-50A. The magnetization curve of the laminates for $f = 50\,\text{Hz}$ given in Table 3.1 was provided by the manufacturer and is shown in Figure 3.3. Looking at the magnetization curve, saturation occurs at about $B_{\text{sat}} = 1.50\,\text{T}$.

The dimensions of one laminate are $H \times W = 500\,\text{mm} \times 94\,\text{mm}$ and its thickness d equals to $0.50\,\text{mm}$. The width of an iron stack in direction of the lamination was measured to be $93.70\,\text{mm}$, therefore the cross-section of the core is almost a square, see Figure 3.5. Between the laminates there is an average gap of $d_0 = 0.01\,\text{mm}$ which yields a fill factor of 98%. The electric conductivity σ_m is assumed to be $2.08 \times 10^6\,\text{S/m}$.

3.2.3 Coils

A coil consists of two layers of 60 turns ($N_c = 120$) mounted on a cardboard cylinder. The layers are separated with a $4\,\text{mm}$ gap. The distance is kept by small pieces of wood, see Figure 3.4. The height h of the coil is $162\,\text{mm}$. A copper wire with a diameter of $3.00\,\text{mm}$ and a lacquer coat with a thickness of $0.10\,\text{mm}$ is used for the windings.

In Figure 3.6 the layout of the benchmark is drawn. Following the procedure of section 3.1 using the above specifications, the air gap width was selected to be $l_0 = 0.50\,\text{mm}$. This leaves enough space for a search coil to be inserted in the air gape.

B in T	H in A m^{-1}
0	0
0.02	20
0.1	40.1
0.2	52.5
0.3	60.8
0.4	68.1
0.5	75.2
0.6	82.5
0.7	90.4
0.8	99.3

B in T	H in A m^{-1}
0.9	110
1	125
1.1	146
1.2	181
1.3	251
1.4	443
1.5	1,110
1.6	2,900
1.7	6,020
1.8	10,600

Table 3.1. Magnetization curve of M400-50A provided by the manufacturer.

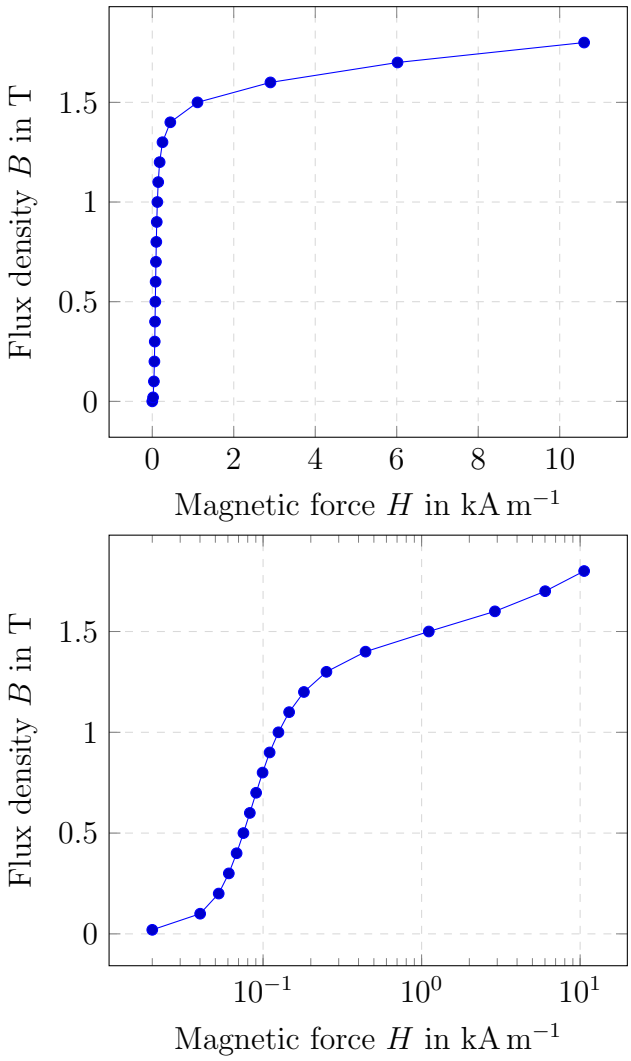

Figure 3.3. Magnetization curve in linear and logarithmic scaling of H.

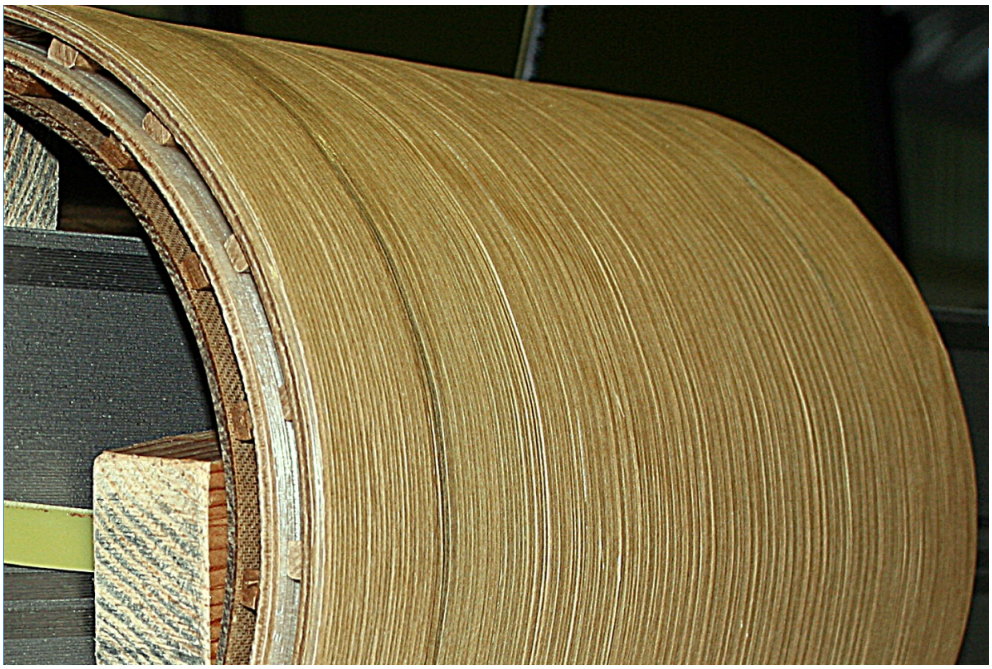

Figure 3.4. Photo of one coil.

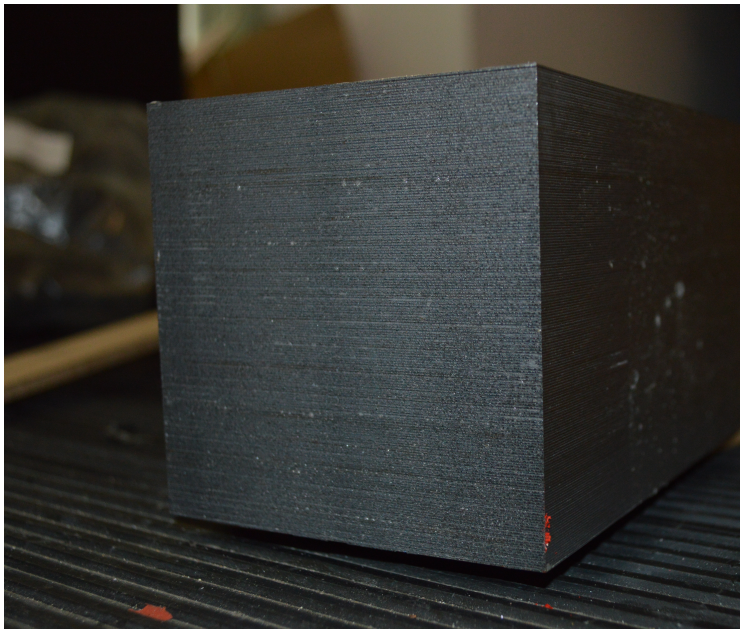

Figure 3.5. Photo of the iron stack.

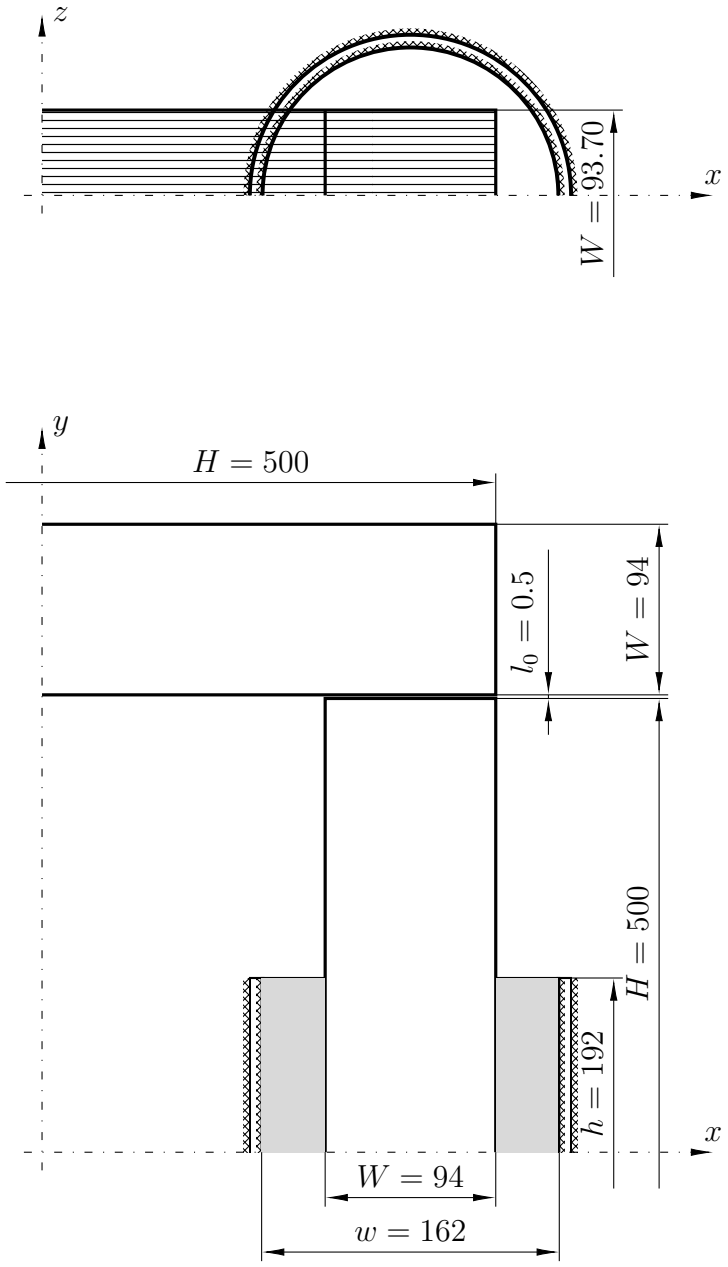

Figure 3.6. Sketch of the benchmark setup. Dimension are in mm.

4 FEM-Model

4.1 Time-stepping

In the nonlinear case, the time dependency of the PDE (2.1.28) does not lend itself to the complex method with a singular frequency. Indeed, when the excitation is harmonic, the solution will still be periodic but not harmonic anymore. A common possibility for the numerical treatment of the nonlinear problem is the harmonic balance or multiharmonic method, see [15] or [16].

In this work, the time domain solution $\boldsymbol{A}(t)$ is computed on a temporal discretization of the time interval $[t_0, t_N]$ with N_t time instants

$$t_k = k\Delta t. \tag{4.1.1}$$

with a fixed time step Δt. The time derivative is discretized with the backward euler method

$$\frac{\partial \boldsymbol{A}}{\partial t}(t_k) \approx \frac{\boldsymbol{A}(t_k) - \boldsymbol{A}(t_{k-1})}{\Delta t}. \tag{4.1.2}$$

Hereinafter, for each time instant t_k the following simple notation

$$\boldsymbol{A} := \boldsymbol{A}(t_k) \tag{4.1.3}$$

$$\boldsymbol{A}_{\text{old}} := \boldsymbol{A}(t_{k-1}) \tag{4.1.4}$$

will be used.

Applying (4.1.2) to the time-derivative in the weak formulation (2.3.3) yields

$$\int_\Omega \nu \operatorname{curl} \boldsymbol{A} \cdot \operatorname{curl} \boldsymbol{v} \,\mathrm{d}\Omega + \int_\Omega \frac{\sigma}{\Delta t} \boldsymbol{A} \cdot \boldsymbol{v} \,\mathrm{d}\Omega = \int_\Omega \boldsymbol{J}_0 \cdot \boldsymbol{v} \,\mathrm{d}\Omega + \int_\Omega \frac{\sigma}{\Delta t} \boldsymbol{A}_{\text{old}} \cdot \boldsymbol{v} \,\mathrm{d}\Omega \tag{4.1.5}$$

and the corresponding FE equation system is

$$\mathbf{S}\boldsymbol{u} + \widetilde{\mathbf{M}}\boldsymbol{u} = \boldsymbol{f} + \widetilde{\mathbf{M}}\boldsymbol{u}_{\text{old}} \tag{4.1.6}$$

with the new mass matrix

$$\widetilde{\mathbf{M}} := \frac{1}{\Delta t}\mathbf{M}. \tag{4.1.7}$$

In each time instant the FE equation system (4.1.6) has to be solved. The approximation (4.1.2) introduces a discretization error which decreases with Δt.

4.2 Nonlinear problem

4.2.1 Derivation from minimization problem

In some cases the weak form of a PDE can be derived form a minimization problem

$$\min_{\boldsymbol{A}} J(\boldsymbol{A}), \tag{4.2.1}$$

with some functional $\boldsymbol{J}$. This functional can often be interpreted as an energy. This approach allows the use of methods for optimization problems. For example the line search method can be used to determine a relaxation parameter for the Newton method, to ensure monotonous convergence of the iterative algorithm.

For the ECP the corresponding functional is given as

$$J(\boldsymbol{A}) = \int_\Omega w(|\operatorname{curl}\boldsymbol{A}|)\,\mathrm{d}\Omega + \int_\Omega \frac{\sigma}{2\Delta t}\boldsymbol{A}^{\mathrm{T}}\boldsymbol{A}\,\mathrm{d}\Omega - \int_\Omega \boldsymbol{J}_{\boldsymbol{0}}^{\mathrm{T}}\boldsymbol{A}\,\mathrm{d}\Omega - \int_\Omega \frac{\sigma}{\Delta t}\boldsymbol{A}_{\mathrm{old}}^{\mathrm{T}}\boldsymbol{A}\,\mathrm{d}\Omega \tag{4.2.2}$$

The first integral in (4.2.2) is the magnetic field energy, where

$$w(B) = \int_0^B H(B')\,\mathrm{d}B' \tag{4.2.3}$$

is the energy density for $B = |\operatorname{curl}\boldsymbol{A}|$. For linear problems with the material relation (2.1.17) $w = B^2/(2\mu)$ holds and for nonlinear problems w is obtained from the magnetization curve. Additional terms for Neumann boundary conditions have to be used for the complete BVP. They are omitted for the sake of conciseness.

A necessary condition for the existence of a minimum $\boldsymbol{A}^*$ is, that the solution is a stationary point of the functional. In a stationary solution the variation of the functional

$$\delta J(\boldsymbol{A};\boldsymbol{v}) := \lim_{\eta\to 0}\frac{J(\boldsymbol{A}+\eta\boldsymbol{v}) - J(\boldsymbol{v})}{\eta} \tag{4.2.4}$$

must be zero for every direction $\boldsymbol{v}$. The derivative is

$$\begin{aligned}\frac{\partial}{\partial\eta}J(\boldsymbol{A}+\eta\boldsymbol{v}) = \frac{\partial}{\partial\eta}\Bigg(&\int_\Omega w\big(|\operatorname{curl}(\boldsymbol{A}+\eta\boldsymbol{v})|\big)\,\mathrm{d}\Omega + \int_\Omega \frac{\sigma}{2\Delta t}(\boldsymbol{A}+\eta\boldsymbol{v})^{\mathrm{T}}(\boldsymbol{A}+\eta\boldsymbol{v})\,\mathrm{d}\Omega \\ &- \int_\Omega \boldsymbol{J}_{\boldsymbol{0}}^{\mathrm{T}}(\boldsymbol{A}+\eta\boldsymbol{v})\,\mathrm{d}\Omega - \int_\Omega \frac{\sigma}{\Delta t}\boldsymbol{A}_{\mathrm{old}}^{\mathrm{T}}(\boldsymbol{A}+\eta\boldsymbol{v})\,\mathrm{d}\Omega\Bigg) = \\ \int_\Omega \frac{\partial}{\partial\eta}w\big(|\operatorname{curl}(\boldsymbol{A}+\eta\boldsymbol{v})|\big)\,\mathrm{d}\Omega &+ \int_\Omega \frac{\sigma}{\Delta t}\boldsymbol{A}\cdot\boldsymbol{v}\,\mathrm{d}\Omega - \int_\Omega \boldsymbol{J}_{\boldsymbol{0}}\cdot\boldsymbol{v}\,\mathrm{d}\Omega - \int_\Omega \frac{\sigma}{\Delta t}\boldsymbol{A}_{\mathrm{old}}\cdot\boldsymbol{v}\,\mathrm{d}\Omega\end{aligned} \tag{4.2.5}$$

and using the chain rule yields

$$\frac{\partial}{\partial\eta}w\big(|\operatorname{curl}(\boldsymbol{A}+\eta\boldsymbol{v})|\big) = w'\big(|\operatorname{curl}(\boldsymbol{A}+\eta\boldsymbol{v})|\big)\frac{\operatorname{curl}(\boldsymbol{A}+\eta\boldsymbol{v})}{|\operatorname{curl}(\boldsymbol{A}+\eta\boldsymbol{v})|}\cdot\operatorname{curl}\boldsymbol{v}. \tag{4.2.6}$$

Evaluating at $\eta = 0$ and setting (4.2.5) to zero leads to the weak form of the nonlinear ECP

$$\int_\Omega \frac{\sigma}{\Delta t}\boldsymbol{A}\cdot\boldsymbol{v}\,\mathrm{d}\Omega + \int_\Omega w'\big(|\operatorname{curl}\boldsymbol{A}|\big)\frac{\operatorname{curl}\boldsymbol{A}}{|\operatorname{curl}\boldsymbol{A}|}\cdot\operatorname{curl}\boldsymbol{v}\,\mathrm{d}\Omega = \int_\Omega \boldsymbol{J_0}\cdot\boldsymbol{v}\,\mathrm{d}\Omega + \int_\Omega \frac{\sigma}{\Delta t}\boldsymbol{A}_{\mathrm{old}}\cdot\boldsymbol{v}\,\mathrm{d}\Omega. \tag{4.2.7}$$

For linear problems, (4.2.7) is equal to the linear weak form (4.1.5).

4.2.2 Newton's method for nonlinear FEM

The FEM equation system for the nonlinear weak form can be denoted as

$$\widetilde{\mathbf{S}}(\boldsymbol{u})\boldsymbol{u} + \widetilde{\mathbf{M}}\boldsymbol{u} = \boldsymbol{f} + \widetilde{\mathbf{M}}\boldsymbol{u}_{\mathrm{old}} \tag{4.2.8}$$

which is nonlinear in $\boldsymbol{u}$. To solve this nonlinear equation system Newton's method is used, because of its high convergence rate. A series $(\boldsymbol{u}_i)$ is calculated, which under some conditions fulfills

$$\lim_{i\to\infty}\boldsymbol{u}_i = \boldsymbol{u}^*. \tag{4.2.9}$$

The iteration is defined by the recursion

$$\boldsymbol{u}_{i+1} := \boldsymbol{u}_i - \alpha\left(D(\boldsymbol{u}_i)\right)^{-1}\boldsymbol{d}(\boldsymbol{u}_i) = \boldsymbol{u}_i + \alpha\boldsymbol{w}_i. \tag{4.2.10}$$

Here $D(\boldsymbol{u}_i)$ denotes the Jacobian matrix of the vector-valued function $\boldsymbol{d}$

$$D(\boldsymbol{u}) = (\nabla\boldsymbol{d})^{\mathrm{T}}(\boldsymbol{u}) = \left(\frac{\mathrm{d}}{\mathrm{d}\boldsymbol{u}}\boldsymbol{d}\right)(\boldsymbol{u}) \tag{4.2.11}$$

evaluated at $\boldsymbol{u}_i$ with the residuum

$$\boldsymbol{d}(\boldsymbol{u}) = \widetilde{\mathbf{S}}(\boldsymbol{u})\boldsymbol{u} + \widetilde{\mathbf{M}}\boldsymbol{u} - \widetilde{\mathbf{M}}\boldsymbol{u}_{\mathrm{old}} - \boldsymbol{f} \tag{4.2.12}$$

One has to solve the linear equation system

$$D(\boldsymbol{u}_i)\boldsymbol{w}_i = -\boldsymbol{d}(\boldsymbol{u}_i) \tag{4.2.13}$$

either directly or iteratively, to obtain the Newton direction $\boldsymbol{w}_i$. To evaluate $\boldsymbol{d}(\boldsymbol{u})$ the vector

$$\widetilde{\mathbf{S}}(\boldsymbol{u})\boldsymbol{u} = \int_\Omega \begin{pmatrix} (\operatorname{curl}\boldsymbol{\varphi}_1)^{\mathrm{T}} \\ \vdots \\ (\operatorname{curl}\boldsymbol{\varphi}_{N_{\mathrm{DoF}}})^{\mathrm{T}} \end{pmatrix} \boldsymbol{H}(\boldsymbol{u})\,\mathrm{d}\Omega, \tag{4.2.14}$$

with $\boldsymbol{H}(\boldsymbol{u})$ evaluated according to the magnetization curve, is assembled. Inserting (4.2.12) into (4.2.11) yields

$$D(\boldsymbol{u}) = \Big(\nabla(\widetilde{\mathbf{S}}(\boldsymbol{u})\boldsymbol{u}\Big))^{\mathrm{T}} + \widetilde{\mathbf{M}} \tag{4.2.15}$$

and the linearization of $\widetilde{\mathbf{S}}(\boldsymbol{u})$ is obtained by

$$\begin{aligned}\Big(\nabla(\widetilde{\mathbf{S}}(\boldsymbol{u})\boldsymbol{u}\Big))^{\mathrm{T}} = \\ \frac{\mathrm{d}}{\mathrm{d}\boldsymbol{u}}\int_{\Omega}\begin{pmatrix}(\operatorname{curl}\boldsymbol{\varphi}_1)^{\mathrm{T}}\\ \vdots \\ (\operatorname{curl}\boldsymbol{\varphi}_{N_{\mathrm{DoF}}})^{\mathrm{T}}\end{pmatrix}\boldsymbol{H}(\boldsymbol{u})\,\mathrm{d}\Omega = \int_{\Omega}\begin{pmatrix}(\operatorname{curl}\boldsymbol{\varphi}_1)^{\mathrm{T}}\\ \vdots \\ (\operatorname{curl}\boldsymbol{\varphi}_{N_{\mathrm{DoF}}})^{\mathrm{T}}\end{pmatrix}\frac{\mathrm{d}\boldsymbol{H}}{\mathrm{d}\boldsymbol{B}}\frac{\mathrm{d}}{\mathrm{d}\boldsymbol{u}}\boldsymbol{B}(\boldsymbol{u})\,\mathrm{d}\Omega = \\ \int_{\Omega}\begin{pmatrix}(\operatorname{curl}\boldsymbol{\varphi}_1)^{\mathrm{T}}\\ \vdots \\ (\operatorname{curl}\boldsymbol{\varphi}_{N_{\mathrm{DoF}}})^{\mathrm{T}}\end{pmatrix}\frac{\mathrm{d}\boldsymbol{H}}{\mathrm{d}\boldsymbol{B}}\left(\operatorname{curl}\boldsymbol{\varphi}_1,\quad \ldots\quad ,\operatorname{curl}\boldsymbol{\varphi}_{N_{\mathrm{DoF}}}\right)\,\mathrm{d}\Omega \end{aligned} \tag{4.2.16}$$

The magnetic field strength for an isotropic material is

$$\boldsymbol{H}(\boldsymbol{B}) = H(B)\frac{\boldsymbol{B}}{|\boldsymbol{B}|}. \tag{4.2.17}$$

Considering each component h_i with $i \in \{1,2,3\}$ of $\boldsymbol{H}$ individually

$$h_i(\boldsymbol{B}) = H(B)\frac{b_i}{|\boldsymbol{B}|} \tag{4.2.18}$$

the derivative with respect to a component b_j of $\boldsymbol{B}$ is

$$\begin{aligned}\frac{\partial h_i}{\partial b_j} = H'(|\boldsymbol{B}|)\frac{b_j}{|\boldsymbol{B}|}\frac{b_i}{|\boldsymbol{B}|} + H(|\boldsymbol{B}|)\frac{\frac{\partial b_i}{\partial b_j}|\boldsymbol{B}| - b_i\frac{b_j}{|\boldsymbol{B}|}}{|\boldsymbol{B}|^2} = \\ \left(H'(|\boldsymbol{B}|) - \frac{H(|\boldsymbol{B}|)}{|\boldsymbol{B}|}\right)\frac{b_i}{|\boldsymbol{B}|}\frac{b_j}{|\boldsymbol{B}|} + \frac{H(|\boldsymbol{B}|)}{|\boldsymbol{B}|}\frac{\partial b_i}{\partial b_j}.\end{aligned}$$

Together this yields

$$\frac{\mathrm{d}\boldsymbol{H}}{\mathrm{d}\boldsymbol{B}} = \begin{pmatrix}\frac{\partial h_1}{\partial b_1} & \frac{\partial h_1}{\partial b_2} & \frac{\partial h_1}{\partial b_3}\\ \frac{\partial h_2}{\partial b_1} & \frac{\partial h_2}{\partial b_2} & \frac{\partial h_2}{\partial b_3}\\ \frac{\partial h_3}{\partial b_1} & \frac{\partial h_3}{\partial b_2} & \frac{\partial h_3}{\partial b_3}\end{pmatrix} = \left(H'(|\boldsymbol{B}|) - \frac{H(|\boldsymbol{B}|)}{|\boldsymbol{B}|}\right)\frac{\boldsymbol{B}}{|\boldsymbol{B}|}\frac{\boldsymbol{B}^T}{|\boldsymbol{B}|} + \frac{H(|\boldsymbol{B}|)}{|\boldsymbol{B}|}\mathbf{E} \tag{4.2.19}$$

or

$$\frac{\mathrm{d}\boldsymbol{H}}{\mathrm{d}\boldsymbol{B}} = \left(\nu^{\mathrm{d}} - \frac{H}{B}\right)\boldsymbol{e}_B\boldsymbol{e}_B^{\mathrm{T}} + \frac{H}{B}\mathbf{E} \tag{4.2.20}$$

where ν^{d} is the derivative of the magnetization curve with respect to B and $\boldsymbol{e}_B$ is the direction vector of $\boldsymbol{B}$.

4.2.3 Line search

As it was shown before, solving (4.2.8) is equivalent to finding the minimum of $J(\boldsymbol{u})$. Therefore in each Newton step, after computing the Newton direction $\boldsymbol{w}_i$, a one dimensional minimization problem has to be solved to find the minimum of $J(\boldsymbol{u})$ in the direction $\boldsymbol{w}_i$ with respect to α

$$\min_{\alpha} J(\boldsymbol{u}_i + \alpha\boldsymbol{w}_i). \tag{4.2.21}$$

In contrast to [17], where an optimal α is calculated in each Newton step, a simple line search technique was used in this work to determine some value α, satisfying

$$J(\boldsymbol{u}_{i+1}) < J(\boldsymbol{u}_i). \tag{4.2.22}$$

In each Newton step starting from $\alpha_0 = 1$ the relaxation parameter was reduced by the formula

$$\alpha_{j+1} = \frac{1}{2}\alpha_j \tag{4.2.23}$$

until

$$J(\boldsymbol{u}_i + \alpha_{j+1}) > J(\boldsymbol{u}_i + \alpha_j). \tag{4.2.24}$$

The resulting α_j was chosen as the relaxation parameter for the Newton step. This simple approach is enough to guarantee a monotonous decrease of $J(\boldsymbol{u}_{i+1})$.

4.3 Network coupling

In the previous sections it was assumed that $\boldsymbol{J}_0$ was given. Now, a voltage source which drives the coil shall be incorporated in the model. In this setting the coil is coupled to a network with a known clamping voltage U and $\boldsymbol{J}_0$ is treated as an unknown. This method was introduced in [18] and in [19]. Like before, it is assumed that the current in the wire is uniformly distributed (skin and proximity effects are neglected). In addition the wires are packed sufficiently close, so that a smooth current density distribution can be assumed. In this case, $\boldsymbol{J}_0$ is uniquely defined by the current I with

$$\boldsymbol{J}_0 = \frac{N_c I}{A_c}\boldsymbol{n}_c. \tag{4.3.1}$$

The numbers of windings N_c, the cross-section A_c and the direction of the turns $\boldsymbol{n}_c$ of the coil are combined in the vector function

$$\boldsymbol{\tau} := \frac{N_\mathrm{c}}{A_\mathrm{c}}\boldsymbol{n}_\mathrm{c}, \tag{4.3.2}$$

which will be called *turns density*.

The applied voltage U, which equals is the sum of the induction voltage and the voltage drop due to the resistance (the resistance of the wire plus a serial resistor), leads to the network equation

$$\int\limits_{C_{N_c}} \frac{\mathrm{d}\boldsymbol{A}}{\mathrm{d}t} \cdot \boldsymbol{n}_\mathrm{c}\,\mathrm{d}l + IR = U \tag{4.3.3}$$

where C_{N_c} is the path along the wire of the coil and C_c is a single turn. The line integral in (4.3.3) is transformed to an integral over the domain of the coil Ω_c by

$$\int\limits_{C_{N_c}} \frac{\mathrm{d}\boldsymbol{A_c}}{\mathrm{d}t} \cdot \boldsymbol{n}_c\,\mathrm{d}l = \frac{N_c}{A_c}\int\limits_S\int\limits_{C_c} \frac{\mathrm{d}\boldsymbol{A}}{\mathrm{d}t} \cdot \boldsymbol{n}_c\,\mathrm{d}l\,\mathrm{d}S = \int\limits_{\Omega_c} \frac{\mathrm{d}\boldsymbol{A}}{\mathrm{d}t} \cdot \frac{N_c}{A_c}\boldsymbol{n}_c\,\mathrm{d}\Omega, \tag{4.3.4}$$

which, using (4.3.2), leads to

$$\int_{\Omega_c} \frac{\mathrm{d}\boldsymbol{A}}{\mathrm{d}t} \boldsymbol{\tau} \,\mathrm{d}\Omega + RI = U. \tag{4.3.5}$$

Inserting $\boldsymbol{J_0} = I\boldsymbol{\tau}$ into the weak formulation (4.1.2)

$$\int_{\Omega} \nu \operatorname{curl} \boldsymbol{A} \cdot \operatorname{curl} \boldsymbol{v} \,\mathrm{d}\Omega + \int_{\Omega} \frac{\sigma}{\Delta t} \boldsymbol{A} \cdot \boldsymbol{v} \,\mathrm{d}\Omega = I \int_{\Omega} \boldsymbol{\tau} \cdot \boldsymbol{v} \,\mathrm{d}\Omega + \int_{\Omega} \frac{\sigma}{\Delta t} \boldsymbol{A}_{\mathrm{old}} \cdot \boldsymbol{v} \,\mathrm{d}\Omega \tag{4.3.6}$$

and applying the discretization of the time-derivative (4.1.2) to (4.3.5)

$$\int_{\Omega} \frac{\boldsymbol{A} - \boldsymbol{A}_{\mathrm{old}}}{\Delta t} \boldsymbol{\tau} \,\mathrm{d}\Omega + RI = U \tag{4.3.7}$$

yields a system of equations for the ECP with network coupling. Using the new load vector

$$\widetilde{\boldsymbol{f}} := \int_{\Omega} \begin{pmatrix} (\boldsymbol{\varphi}_1)^{\mathrm{T}} \\ \vdots \\ (\boldsymbol{\varphi}_{N_{\mathrm{DoF}}})^{\mathrm{T}} \end{pmatrix} \boldsymbol{\tau} \,\mathrm{d}\Omega \tag{4.3.8}$$

the FEM equation system

$$\widetilde{\mathbf{S}}(\boldsymbol{u})\boldsymbol{u} + \widetilde{\mathbf{M}}\boldsymbol{u} = I\widetilde{\boldsymbol{f}} + \widetilde{\mathbf{M}}\boldsymbol{u}_{\mathrm{old}} \tag{4.3.9}$$

corresponding to (4.3.6) is obtained. The network equation 4.3.7 can be expressed as

$$\widetilde{\boldsymbol{f}}^{\mathrm{T}} (\boldsymbol{u} - \boldsymbol{u}_{\mathrm{old}}) + \Delta t RI = \Delta t U. \tag{4.3.10}$$

For each time instant the extended equation system

$$\begin{bmatrix} \widetilde{\mathbf{S}}(\boldsymbol{u}) + \widetilde{\mathbf{M}} & -\widetilde{\boldsymbol{f}} \\ -\widetilde{\boldsymbol{f}}^{\mathrm{T}} & -\Delta t R \end{bmatrix} \begin{bmatrix} \boldsymbol{u} \\ I \end{bmatrix} = \begin{bmatrix} \widetilde{\mathbf{M}}\boldsymbol{u}_{\mathrm{old}} \\ -\Delta t U - \widetilde{\boldsymbol{f}}^{\mathrm{T}}\boldsymbol{u}_{\mathrm{old}} \end{bmatrix} \tag{4.3.11}$$

has to be solved for a given U. The coefficient matrix of the extend equation system does not have the typical structure of a FE equation system anymore. Therefore the existing precondition techniques would have to be modified. To avoid this a separated Newton method is used instead.

4.3.1 Separated Newton method

First, a Newton step is performed for a starting value of $\boldsymbol{u}_0 = \boldsymbol{u}_{\mathrm{old}}$ and $I_0 = I_{\mathrm{old}}$

$$\boldsymbol{u}_1 = \boldsymbol{u}_0 + \alpha \boldsymbol{w}_0 \tag{4.3.12}$$

where $\boldsymbol{w}_0$ is calculated using the field equation (4.3.9) in a similar fashion to (4.2.13) with $I = I_0$. Afterwards, a Newton step is performed for the network equation (4.3.10) with $\boldsymbol{u} = \boldsymbol{u}_1$:

$$I_1 = I_0 - \frac{1}{\widetilde{\boldsymbol{f}}^{\mathrm{T}} \frac{\mathrm{d}(\boldsymbol{u})}{\mathrm{d}I} + \Delta t R} \left(\widetilde{\boldsymbol{f}}^{\mathrm{T}} (\boldsymbol{u}_1 - \boldsymbol{u}_{\mathrm{old}}) + \Delta t R I_0 - \Delta t U \right) \tag{4.3.13}$$

To get $\frac{\mathrm{d}(\boldsymbol{u})}{\mathrm{d}I}$ the derivative of (4.3.9) is taken

$$D(\boldsymbol{u}) \frac{\mathrm{d}(\boldsymbol{u})}{\mathrm{d}I} = \widetilde{\boldsymbol{f}} \tag{4.3.14}$$

and the equation system is solved for $\boldsymbol{u} = \boldsymbol{u}_1$. The resulting I_1 is then used for the next Newton step.

4.4 Biot-Savart field

The Biot-Savart law can be exploited to circumvent the meshing of the coils. The magnetic field is separated into a field $\boldsymbol{H}_0$ that is caused by $\boldsymbol{J}_0$ in an infinite homogeneous air domain

$$\operatorname{curl} \boldsymbol{H}_0 = \boldsymbol{J}_0 \tag{4.4.1}$$

and a field $\boldsymbol{H}_m$ to take into account the magnetic medium:

$$\boldsymbol{H} = \boldsymbol{H}_0 + \boldsymbol{H}_m \tag{4.4.2}$$

A known current density distribution $\boldsymbol{J}_0$ yields the Biot-Savart field

$$\boldsymbol{H}_0(\boldsymbol{r}) = \frac{1}{4\pi} \int_{\Omega_c} \frac{\boldsymbol{J}_0(\boldsymbol{r}') \times (\boldsymbol{r} - \boldsymbol{r}')}{|\boldsymbol{r} - \boldsymbol{r}'|^3} \, \mathrm{d}\Omega, \tag{4.4.3}$$

where $\boldsymbol{r}$ denotes the field point and $\boldsymbol{r}'$ denotes the source point, see [20]. For a cylindrical coil with a $\boldsymbol{J}_0$ of constant magnitude, (4.4.3) can be numerically computed with known formulas, see [21]. Eliminating $\boldsymbol{J}_0$ in (2.3.3) with (4.4.1) gives

$$\int_\Omega \nu \operatorname{curl} \boldsymbol{A} \cdot \operatorname{curl} \boldsymbol{v} \, \mathrm{d}\Omega + \frac{\partial}{\partial t} \int_\Omega \sigma \boldsymbol{A} \cdot \boldsymbol{v} \, \mathrm{d}\Omega = \int_\Omega \operatorname{curl} \boldsymbol{H}_0 \cdot \boldsymbol{v} \, \mathrm{d}\Omega. \tag{4.4.4}$$

The right hand side of (4.4.4) is integrated by parts

$$\int_\Omega \operatorname{curl} \boldsymbol{H}_0 \cdot \boldsymbol{v} \, \mathrm{d}\Omega = \int_\Omega \boldsymbol{H}_0 \cdot \operatorname{curl} \boldsymbol{v} \, \mathrm{d}\Omega + \int_\Gamma (\boldsymbol{H}_0 \times \boldsymbol{v}) \cdot \boldsymbol{n} \, \mathrm{d}\Gamma. \tag{4.4.5}$$

The boundary integral in (4.4.5) is neglected for the sake of convenience. Testing with test functions $\boldsymbol{\varphi}_i$ gives the right hand side

$$\boldsymbol{f}_{\mathrm{BS}} = \int_\Omega \begin{pmatrix} (\operatorname{curl} \boldsymbol{\varphi}_1)^{\mathrm{T}} \\ \vdots \\ (\operatorname{curl} \boldsymbol{\varphi}_{N_{\mathrm{DoF}}})^{\mathrm{T}} \end{pmatrix} \boldsymbol{H}_0 \, \mathrm{d}\Omega \tag{4.4.6}$$

of the FEM equation system.

The Biot-Savart law can also be used in case of network coupling, because

$$I\boldsymbol{\tau} = \operatorname{curl} \boldsymbol{H}_0 \tag{4.4.7}$$

holds and it can be equivalently expressed according to (4.4.1) as

$$\boldsymbol{\tau} = \operatorname{curl} \boldsymbol{h}_0, \tag{4.4.8}$$

where $\boldsymbol{h}_0$ is the Biot-Savart field (4.4.3) of the coil for a current $I = 1$. The vector (4.4.6) can be calculated for an arbitrary current I by

$$\boldsymbol{f}_{\mathrm{BS}} = I \int_{\Omega} \begin{pmatrix} (\operatorname{curl} \boldsymbol{\varphi}_1)^{\mathrm{T}} \\ \vdots \\ (\operatorname{curl} \boldsymbol{\varphi}_{N_{\mathrm{DoF}}})^{\mathrm{T}} \end{pmatrix} \boldsymbol{h}_0 \,\mathrm{d}\Omega = I \widetilde{\boldsymbol{f}}_{\mathrm{BS}}. \tag{4.4.9}$$

Inserting (4.4.8) into the network equation (4.3.7) and using integration by parts for

$$-\int_{\Omega} \frac{\mathrm{d}\boldsymbol{A}}{\mathrm{d}t} \cdot \operatorname{curl} \boldsymbol{h}_0 \,\mathrm{d}\Omega = -\int_{\Omega} \operatorname{curl} \frac{\mathrm{d}\boldsymbol{A}}{\mathrm{d}t} \cdot \boldsymbol{h}_0 \,\mathrm{d}\Omega - \int_{\Gamma} \left(\frac{\mathrm{d}\boldsymbol{A}}{\mathrm{d}t} \times \boldsymbol{h}_0 \right) \cdot \boldsymbol{n} \,\mathrm{d}\Gamma, \tag{4.4.10}$$

and neglecting the boundary integral in (4.4.10), leads to

$$-\int_{\Omega} \operatorname{curl} \frac{\mathrm{d}\boldsymbol{A}}{\mathrm{d}t} \cdot \boldsymbol{h}_0 \,\mathrm{d}\Omega + RI = U. \tag{4.4.11}$$

Using the backward euler method (4.1.2) yields

$$-\widetilde{\boldsymbol{f}}_{\mathrm{BS}}^{\mathrm{T}} (\boldsymbol{u} - \boldsymbol{u}_{\mathrm{old}}) + \Delta t R I = \Delta t U. \tag{4.4.12}$$

5 Simulations

The methods in section 4 were integrated into the open-source FEM-library NGSolve and the benchmark was modeled using the specifications discussed in section 3.2. The simulation results presented in section 5.1 will show that the requirements of the benchmark are fulfilled.

At the time of writing this thesis it was not possible to obtain measurements of the benchmark, since the ends of the iron stacks had not been manufactured evenly. The air gaps have a high impact on the reluctance of the magnetic circuit, therefore an exact air gap width is indispensable. As a temporary substitute, a simple set up was arranged, which does suffer from the aforementioned problems. The simple setup was also simulated and the comparison with the measurement results is presented in section 5.2.1.

5.1 Benchmark verification

5.1.1 Mesh and element order

The Netgen mesh generator provides efficient routines for mesh generation with tetrahedral and prismatic elements, including adaptive mesh refinement. However, due to the high number of laminates with very different dimensions (length compared to the thickness) a handmade mesh with rectangular hexahedral elements had to be used, see Figure 5.1.

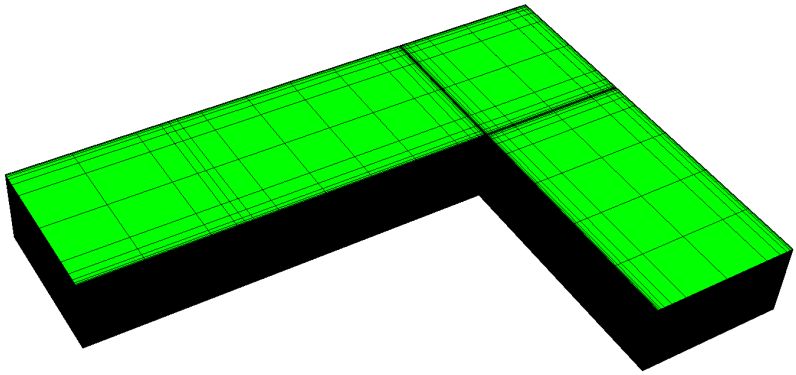

Figure 5.1. The FE mesh of Ω_m.

In this work, no homogenization methods were utilized for the laminated iron cores, meaning that each single laminate was modeled with FEs. Hexahedral edge finite elements of second order were used [22]. The thickness of the laminates were divided subdivided once. A rather coarse mesh suffices in the tangential directions, except along the edges, see Figure 5.2. Likewise, the mesh was refined in areas where a high stray flux is expected. The FE mesh resolves the penetration depth

$$\delta = \sqrt{\frac{1}{\pi f \sigma \mu}} \tag{5.1.1}$$

of the electromagnetic field.

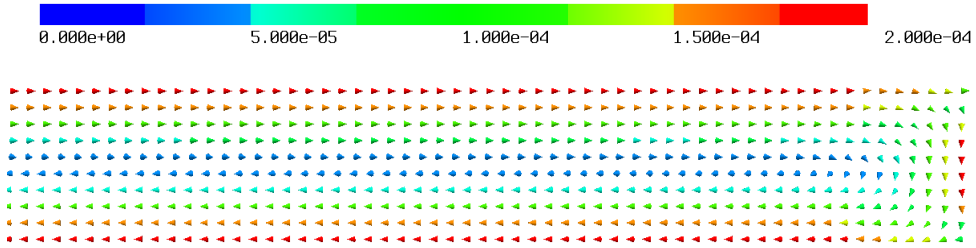

Figure 5.2. Vector plot of $\boldsymbol{A}$ in the cross section of a laminate.

5.1.2 Boundary conditions

On the far boundary homogeneous Neumann conditions (2.1.29a) were prescribed. In order to test if the boundary conditions influence the solution a cross-check with homogeneous Dirichlet boundary conditions (2.1.29b) was performed. If the difference of the solutions in Ω_m for both type of boundary conditions would not have been negligible, the size of Ω would have had to be increased.

The symmetry of the problem was exploited. Thereby only one eight of the problem had to be modeled. This required appropriate boundary conditions on the symmetry planes, see Figure 3.6. The boundary conditions were

$$\operatorname{curl} \boldsymbol{A} \times \boldsymbol{n} = \boldsymbol{0} \quad \text{on the} \quad xy\text{-plane} \tag{5.1.2a}$$

$$\boldsymbol{A} \times \boldsymbol{n} = \boldsymbol{0} \quad \text{on the} \quad xz\text{-plane and the } yz\text{-plane} \tag{5.1.2b}$$

in case of positive coupling and

$$\operatorname{curl} \boldsymbol{A} \times \boldsymbol{n} = \boldsymbol{0} \quad \text{on the} \quad xy\text{-plane and the } yz\text{-plane} \tag{5.1.3a}$$

$$\boldsymbol{A} \times \boldsymbol{n} = \boldsymbol{0} \quad \text{on the} \quad xz\text{-plane} \tag{5.1.3b}$$

in case of negative coupling.

For the Biot-Savart field the integral (4.4.3) had to be evaluated in the whole domain Ω_c of both coils. The values of R and U used in (4.4.12) were set to one eighth of the respective values of the full model.

5.1.3 Results

The field lines of $\boldsymbol{B}$ for both coupling types are shown in Figure 5.3 for one time instant. It is clearly visible, that the stray field is more pronounced in the case of negative coupling. It can also be observed, that the saturation level is achieved in case of positive coupling.

To check the third requirement (see section 3.1) the magnitude of $\boldsymbol{B}$ in the stray field is shown Figure 5.4. The plotted region is 10 mm above the iron stack and at a distance of 10 mm from the coil. The magnitude of the flux density B is in the range of 4 mT to 18 mT and 7 mT to 70 mT for positive and negative coupling, respectively. The region for the measurements was chosen in accordance with the measuring range and spatial resolution of the hall-senor.

The current I with respect to time is shown in Figure 5.5 for both couplings. The limit on the effective value of I attained in section 3.2.1 is not exceeded. In case of positive coupling the higher harmonics are clearly pronounced. This indicates that the saturation level in the iron core is achieved. In contrast, I exhibits no saturation behavior in case of negative coupling.

Figure 5.6 shows I for different starting values of the sinusoidal voltage U. The transient effect is due to the time constant of the impedance consisting of the series resistor and the benchmark. The resistance is high enough for the steady state to be reached after a few periods. The worst case is attained, when the voltage starts with zero value, which leads to a very high inrush current. The overcurrent protection in the laboratory has to be able tolerate the high inrush current.

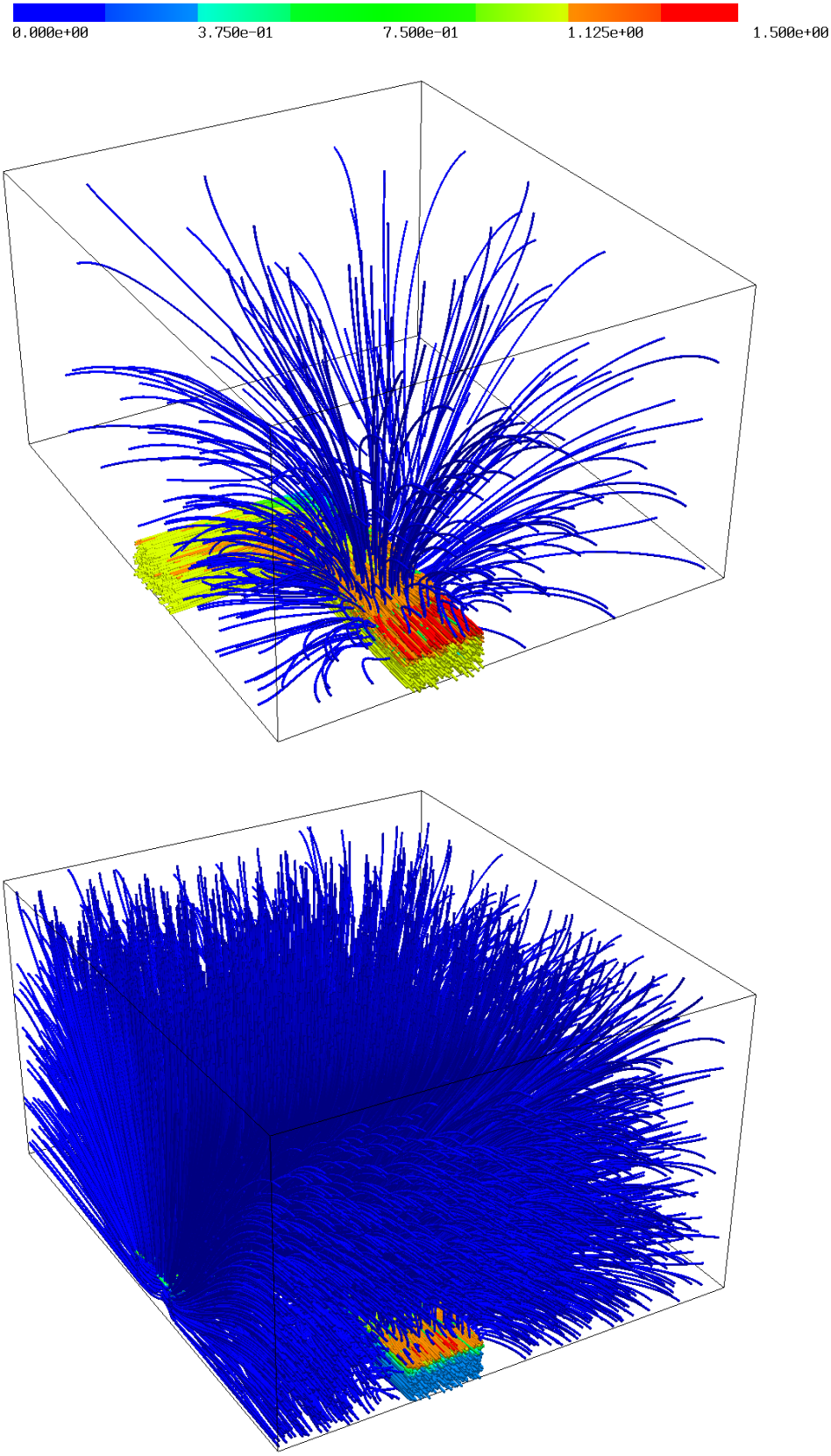

Figure 5.3. Field lines of the $\boldsymbol{B}$-field for positive (above) and negative (below) coupling.

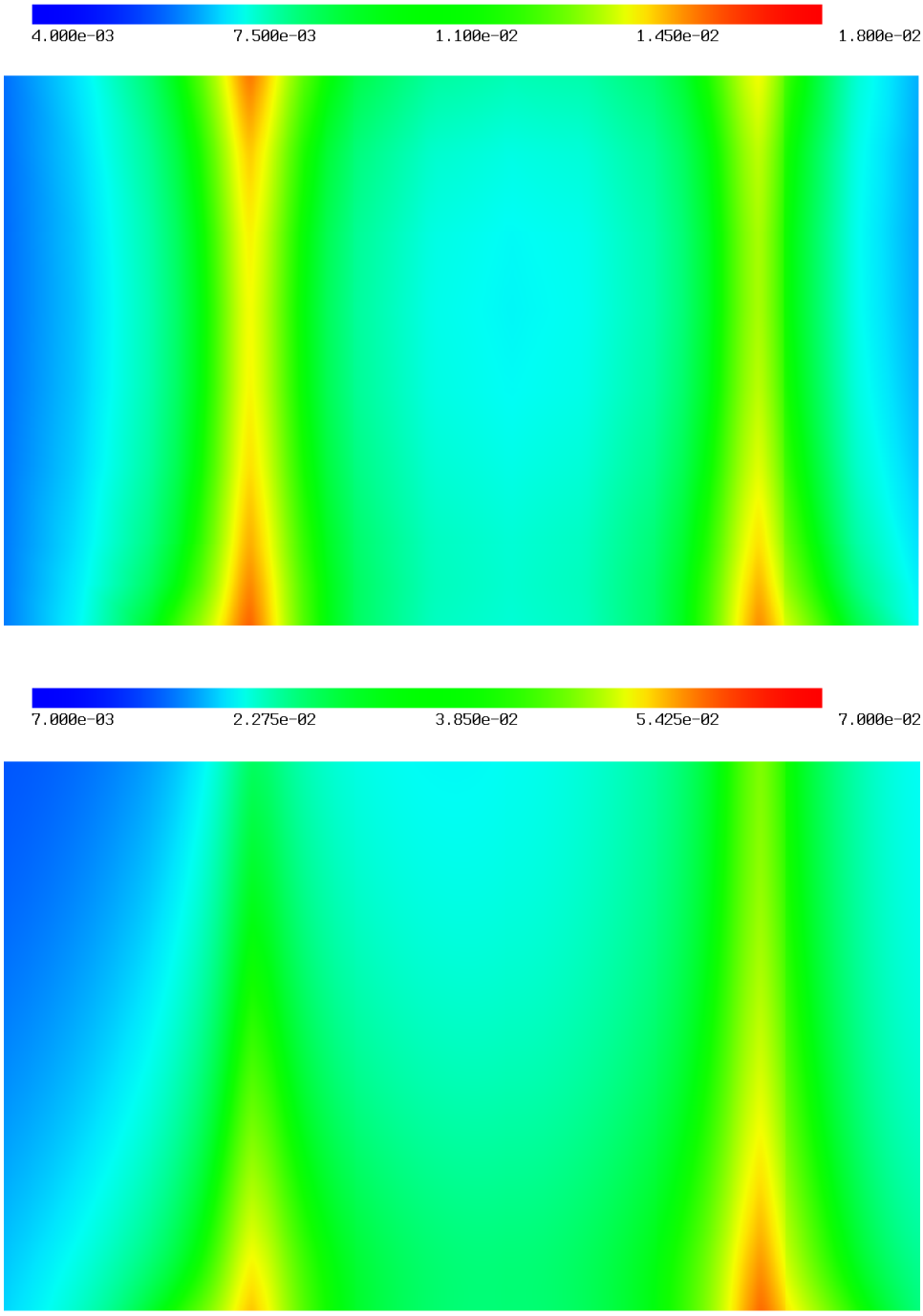

Figure 5.4. B in the stray field for positive (above) and negative (below) coupling.

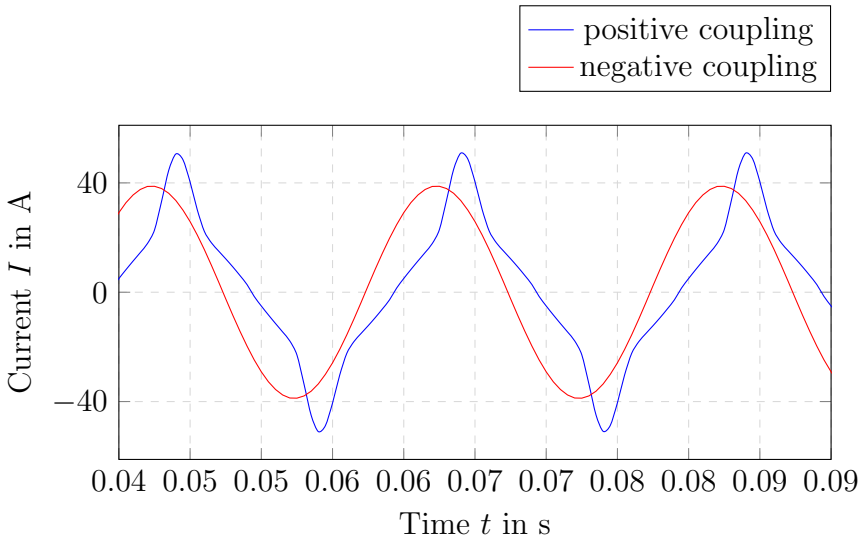

Figure 5.5. Current I for both couplings in the steady state.

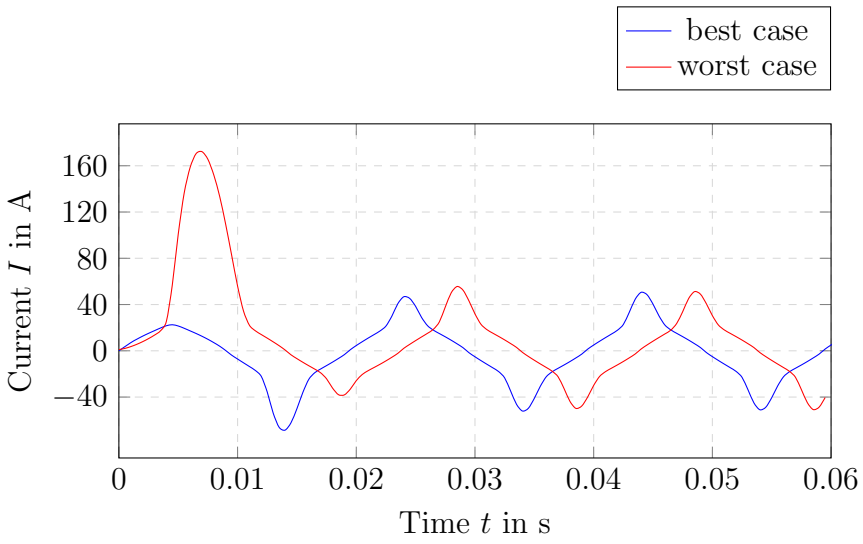

Figure 5.6. Inrush current I for worst and best case initial phase of the input voltage.

5.2 Measurements

A single iron stack and cylindrical coil of the benchmark were used for the simple setup. A power amplifier with a maximum output current of 25 A was used to prescribe a sinusoidal current in the coil. To measure the flux a very thin wire (ø= 0.1 mm) was tightly wound around the center of one outermost laminate and one laminate in the middle of the stack, Figure 5.7.

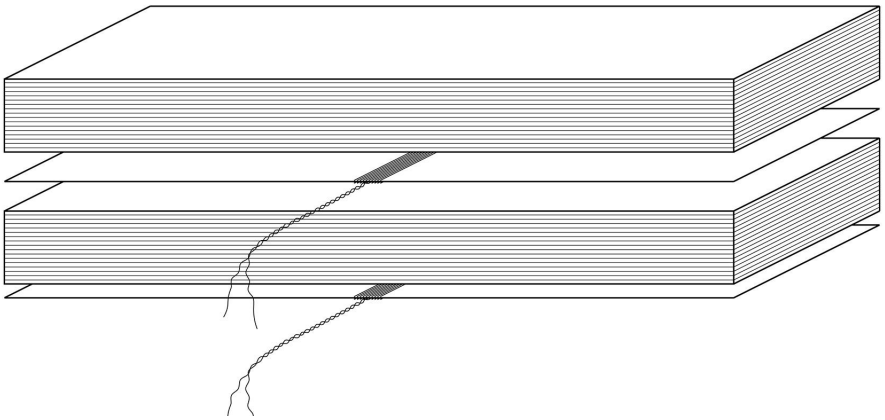

Figure 5.7. The simple setup with a single iron stack and the stylized search coils.

5.2.1 Magnetic flux

The simulation and measurement of Φ in the outer and inner laminate are compared in Figure 5.8 and Figure 5.9. The average flux densities were calculated in order to enable a comparison with the magnetization curve in Figure 3.3.

The simulation result for the middle laminate is in good agreement with the measurement result. Saturation is observed in the simulation and in the measurement for the outer laminate, but there is a significant deviation in the behavior with respect to time.

This difference can be explained by the fact that the magnetization curve is only a simple model of the real material. The magnetization curve is convex-concave for small values of B as observed in Figure 3.3, which causes the deviation between simulation and measurement at the zero-crossing as observed Figure 5.9. The measurement is consistent with the behavior of the hysteresis loop of a ferromagnetic material, see Figure 2.3.

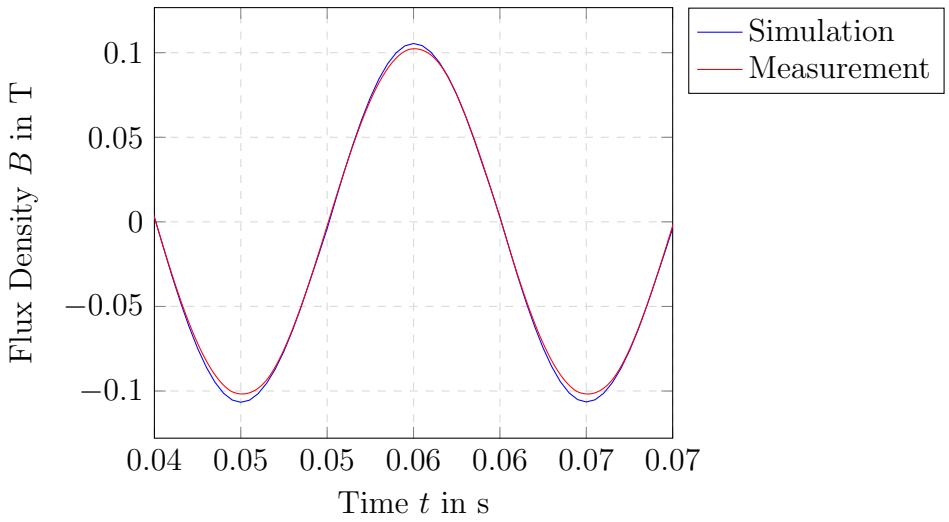

Figure 5.8. Comparison of the magnetic flux in the laminate in the center.

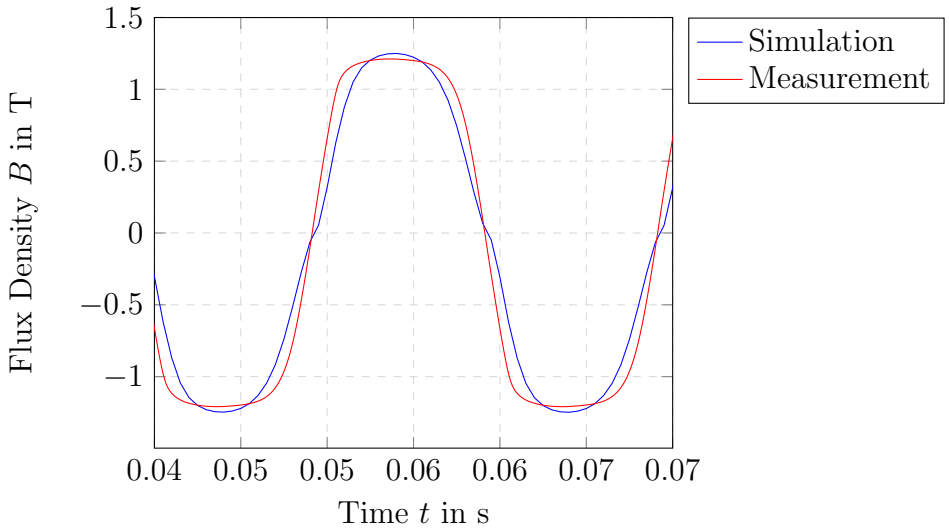

Figure 5.9. Comparison of the magnetic flux in the outermost laminate.

6 Conclusion and Outlook

The used FE-equation system had over 16000000 degrees of freedom. The computational cost was enormous. Without using a high-performance computer the calculations would have been impossible. The application of FEM to problems with laminated iron cores would clearly benefit tremendously from homogenization methods.

Moreover, since the problem was nonlinear the huge equation system had to be solved in each Newton step. Regardless of whether homogenization methods are employed or not, decreasing the computational time for solving the nonlinear problem is of great importance. With regard to this improvements on the methods presented in section 4 should be made.

First of all, solving the network coupled problem with a separated Newton method had the drawback that the FE equation system had to be solved two times in each Newton step. One possible focus of future work would be to develop a preconditioning techniques for equation systems like (4.3.11) to eliminate the separation. Furthermore, the steady state solution was obtained by a time-stepping method. Various techniques could be employed to decrease the computation time to reach the steady state, see [23]. Nonetheless this is an unsatisfactory method, because many periods have to be calculated which are eventually discarded. The multi-harmonics method might be preferable.

The measurements on the simple setup showed that the nonlinear behavior can be modeled using the magnetization curve, resulting only in moderate errors. For accurate results, which are to be realized with this experimental benchmark, a more detailed model is necessary. This includes the consideration of hysteresis, for example with a Preisach model as shown for example in [24].

The next step is the construction of the measuring arrangement using a hall-senor and search coils as presented in section 5.2.1. The measurements will be carried out with the highest possible accuracy. Afterwards, the reference solution will be calculated. During this process, the model of the benchmark will be improved until satisfactory agreement with the measurements is achieved. The measurements as well as the simulation data will be published to the scientific community and will hopefully benefit the advancement of FEM for computational electromagnetics.

List of Figures

1.1 Eddy current simulation in a transformer with Netgen/NGSolve. 11

2.1 Interface Γ_i between the subdomains Ω_1 and Ω_2 with normal vector $\boldsymbol{n}$ and tangential vector $\boldsymbol{t}$. 13
2.2 Bounded domain $\Omega = \Omega_0 \cup \Omega_m$ with the boundary $\Gamma = \Gamma_{\boldsymbol{H}} \cup \Gamma_{\boldsymbol{B}}$. 15
2.3 Characteristic behavior of the ferromagnetic material. 18
2.4 Commutation curve of a laminate measured with an Epstein frame [13]. . 18

3.1 Design of the benchmark with four iron stacks (blue) and two coils (green). 22
3.2 Network coupling of the benchmark with an AC voltage source U_0 and a series resistor R. 23
3.3 Magnetization curve in linear and logarithmic scaling of H. 26
3.4 Photo of one coil. 27
3.5 Photo of the iron stack. 27
3.6 Sketch of the benchmark setup. Dimension are in mm. 28

5.1 The FE mesh of Ω_m. 37
5.2 Vector plot of $\boldsymbol{A}$ in the cross section of a laminate. 38
5.3 Field lines of the $\boldsymbol{B}$-field for positive (above) and negative (below) coupling. 40
5.4 B in the stray field for positive (above) and negative (below) coupling. . 41
5.5 Current I for both couplings in the steady state. 42
5.6 Inrush current I for worst and best case initial phase of the input voltage. 42
5.7 The simple setup with a single iron stack and the stylized search coils. . . 43
5.8 Comparison of the magnetic flux in the laminate in the center. 44
5.9 Comparison of the magnetic flux in the outermost laminate. 44

List of Tables

3.1 Magnetization curve of M400-50A provided by the manufacturer. 26

Bibliography

[1] K. Hollaus and J. Schöberl. "Multi-scale FEM and magnetic vector potential A for 3D eddy currents in laminated media". In: *COMPEL - The international journal for computation and mathematics in electrical and electronic engineering* 34.5 (2015), pp. 1598–1608.

[2] J. Gyselinck, R. V. Sabariego, and P. Dular. "A nonlinear time-domain homogenization technique for laminated iron cores in three-dimensional finite-element models". In: *IEEE Transactions on Magnetics* 42.4 (2006), pp. 763–766.

[3] H. Kaimori, A. Kameari, and K. Fujiwara. "FEM Computation of Magnetic Field and Iron Loss in Laminated Iron Core Using Homogenization Method". In: *IEEE Transactions on Magnetics* 43.4 (2007), pp. 1405–1408.

[4] Z. Cheng, N. Takahashi, B. Forghani, et al. *TEAM problem 21 family (V. 2009).* `http://www.compumag.org/jsite/team.html`.

[5] K. Hollaus et al. "A Linear FEM Benchmark for the Homogenization of the Eddy Currents in Laminated Media in 3D". In: *IFAC Proceedings Volumes* 45.2 (2012). 7th Vienna International Conference on Mathematical Modelling, pp. 1190–1194.

[6] Y. Takahashi et al. "Proposal for a benchmark model of a laminated iron core and a large-scale and highly accurate magnetic analysis". In: *Electrical Engineering in Japan* 170.1 (2010), pp. 26–35.

[7] I. Sebestyen et al. "Calculation of losses in laminated ferromagnetic materials". In: *IEEE Transactions on Magnetics* 40.2 (2004), pp. 924–927.

[8] G. Haase, M. Kuhn, and U. Langer. "Parallel multigrid 3D Maxwell solvers". In: *Parallel Computing* 27.6 (2001), pp. 761–775.

[9] J. Schöberl. *C++11 Implementation of Finite Elements in NGSolve.* Institute for Analysis and Scientific Computing, TU Wien, 2014.

[10] V. C. Silva, G. Meunier, and A. Foggia. "A 3-D finite-element computation of eddy currents and losses in laminated iron cores allowing for electric and magnetic anisotropy". In: *IEEE Transactions on Magnetics* 31.3 (1995), pp. 2139–2141.

[11] O. Bíró. "Edge element formulations of eddy current problems". In: *Computer Methods in Applied Mechanics and Engineering* 169.3 (1999), pp. 391–405.

[12] G. Fasching. *Werkstoffe für die Elektrotechnik.* 2005.

[13] H. Kettler. "Measurement setups for the hysteretic characterization of high permeable materials". Master's thesis. University of Erlangen Nuernberg, 2007.

[14] M. Jung and U. Langer. *Methode der finiten Elemente für Ingenieure*. Wiesbaden, 2013.

[15] J. Gyselinck et al. "Harmonic-balance finite-element modeling of electromagnetic devices: a novel approach". In: *IEEE Transactions on Magnetics* 38.2 (2002), pp. 521–524.

[16] F. Bachinger, U. Langer, and J. Schöberl. "Numerical analysis of nonlinear multiharmonic eddy current problems". In: *Numerische Mathematik* 100.4 (2005), pp. 593–616.

[17] Y. Okamoto, K. Fujiwara, and R. Himeno. "Exact Minimization of Energy Functional for NR Method With Line-Search Technique". In: *IEEE Transactions on Magnetics* 45.3 (2009), pp. 1288–1291.

[18] P. J. Leonard and D. Rodger. "Voltage forced coils for 3D finite-element electromagnetic models". In: *IEEE Transactions on Magnetics* 24.6 (1988), pp. 2579–2581.

[19] T. Nakata et al. "3-D finite element method for analyzing magnetic fields in electrical machines excited from voltage sources". In: *IEEE Transactions on Magnetics* 24.6 (1988), pp. 2582–2584.

[20] O. Zienkiewicz, J. Lyness, and D. Owen. "Three-dimensional magnetic field determination using a scalar potential–A finite element solution". In: *IEEE Transactions on Magnetics* 13.5 (1977), pp. 1649–1656.

[21] L. Urankar. "Vector potential and magnetic field of current-carrying finite arc segment in analytical form, Part III: Exact computation for rectangular cross section". In: *IEEE Transactions on Magnetics* 18.6 (1982), pp. 1860–1867.

[22] J. Schöberl and S. Zaglmayr. "High order Nédélec elements with local complete sequence properties". In: *COMPEL - The international journal for computation and mathematics in electrical and electronic engineering* 24.2 (2005), pp. 374–384.

[23] W. N. Fu, S. L. Ho, and P. Zhou. "Reduction of Computing Time for Steady-State Solutions of Magnetic Field and Circuit Coupled Problems Using Time-Domain Finite-Element Method". In: *IEEE Transactions on Magnetics* 48.11 (2012), pp. 3363–3366.

[24] O. Bottauscio et al. "Dynamic hysteresis and voltage driven solution of a ferromagnetic laminated core". In: *IEEE Transactions on Magnetics* 36.4 (2000), pp. 1238–1241.

Eidesstaatliche Erklärung

Hiermit erkläre ich, dass die vorliegende Arbeit gemäß dem Code of Conduct – Regeln zur Sicherung guter wissenschaftlicher Praxis (in der aktuellen Fassung des jeweiligen Mitteilungsblattes der TU Wien), insbesondere ohne unzulässige Hilfe Dritter und ohne Benutzung anderer als der angegebenen Hilfsmittel, angefertigt wurde. Die aus anderen Quellen direkt oder indirekt übernommenen Daten und Konzepte sind unter Angabe der Quelle gekennzeichnet. Die Arbeit wurde bisher weder im In– noch im Ausland in gleicher oder in ähnlicher Form in anderen Prüfungsverfahren vorgelegt.

Wien, den 11. November 2016

Haik Jan Silm